

<https://helda.helsinki.fi>

Retrieval of Snow Water Equivalent by the Precipitation Imaging Package (PIP) in the Northern Great Lakes

Tokay, Ali

2022-01-01

Tokay , A , von Lerber , A , Pettersen , C , Kulie , M S , Moisseev , D N & Wolff , D B 2022 , ' Retrieval of Snow Water Equivalent by the Precipitation Imaging Package (PIP) in the Northern Great Lakes ' , Journal of Atmospheric and Oceanic Technology , vol. 39 , no. 1 , pp. 37-54 . <https://doi.org/10.1175/JTECH-D-20-0216.1>

<http://hdl.handle.net/10138/352902>

<https://doi.org/10.1175/JTECH-D-20-0216.1>

publishedVersion

Downloaded from Helda, University of Helsinki institutional repository.

This is an electronic reprint of the original article.

This reprint may differ from the original in pagination and typographic detail.

Please cite the original version.

Retrieval of Snow Water Equivalent by the Precipitation Imaging Package (PIP) in the Northern Great Lakes

ALI TOKAY,^{a,b} ANNAKAISA VON LERBER,^c CLAIRE PETTERSEN,^d MARK S. KULIE,^e DMITRI N. MOISSEEV,^f AND DAVID B. WOLFF^g

^a Joint Center for Earth Systems Technology, University of Maryland, Baltimore County, Baltimore, Maryland

^b NASA Goddard Space Flight Center, Greenbelt, Maryland

^c Finnish Meteorological Institute, Helsinki, Finland

^d Space Science and Engineering Center, University of Wisconsin–Madison, Madison, Wisconsin

^e NOAA/NESDIS/Center for Satellite Applications and Research, Madison, Wisconsin

^f Department of Physics, University of Helsinki, Helsinki, Finland

^g Wallops Flight Facility, NASA Goddard Space Flight Center, Wallops Island, Virginia

(Manuscript received 7 January 2021, in final form 15 June 2021)

ABSTRACT: Performance of the Precipitation Imaging Package (PIP) for estimating the snow water equivalent (SWE) is evaluated through a comparative study with the collocated National Oceanic and Atmospheric Administration National Weather Service snow stake field measurements. The PIP together with a vertically pointing radar, a weighing bucket gauge, and a laser-optical disdrometer was deployed at the NWS Marquette, Michigan, office building for a long-term field study supported by the National Aeronautics and Space Administration's Global Precipitation Measurement mission Ground Validation program. The site was also equipped with a weather station. During the 2017/18 winter, the PIP functioned nearly uninterrupted at frigid temperatures accumulating 2345.8 mm of geometric snow depth over a total of 499 h. This long record consists of 30 events, and the PIP-retrieved and snow stake field measured SWE differed less than 15% in every event. Two of the major events with the longest duration and the highest accumulation are examined in detail. The particle mass with a given diameter was much lower during a shallow, colder, uniform lake-effect event than in the deep, less cold, and variable synoptic event. This study demonstrated that the PIP is a robust instrument for operational use, and is reliable for deriving the bulk properties of falling snow.

KEYWORDS: Snowfall; Cloud microphysics; Instrumentation/sensors

1. Introduction

Precipitation is a key component of the water cycle and its global distribution is measured through a multiplatform effort including ground-based, shipborne, airborne, and spaceborne observations. Among these four platforms, the spaceborne measurements are the primary source for mapping the precipitation globally while the remaining three are the component of the validation efforts.

The National Aeronautics and Space Administration (NASA) Global Precipitation Measurement (GPM) mission and its predecessor, the Tropical Rainfall Measuring Mission (TRMM), map the precipitation globally using their core observatories and constellation satellites, and the Ground Validation (GV) program is an integral component of these missions (Skofronick-Jackson et al. 2017). One of the main differences between the TRMM and GPM missions is the orbital inclination of *Core Observatory* of 35° and 65°, respectively. Field campaigns are integral components of the Earth-observing satellite missions. Several field campaigns were conducted in the tropics and subtropics during TRMM era (Lau et al. 2000) but moved toward mid- to high latitudes where precipitation falls in liquid, mixed, and solid phases during GPM era (Skofronick-Jackson et al. 2015).

Historically, much of our knowledge of mixed and solid phase microphysics relies on the optical array probes on board research aircrafts (Field et al. 2006), while the surface measurements of falling snowflakes have been based on sampling individual particles (Gunn and Marshall 1958) until optical disdrometers became available. Optical disdrometers measure the size and fall velocity of individual mixed and frozen particles with different degrees of uncertainty; however, the complex shape, composition, and orientation bring additional challenges in determining the equivalent diameter of the snowflakes. The commercially available laser-optical Particle Size Velocity (PARSIVEL) and Two-Dimensional Video Disdrometer (2DVD) were originally developed to measure the raindrops. Battaglia et al. (2010) showed the limitations of the snowflake size and fall velocity measurements of snowflakes by PARSIVEL. The 2DVD measures the size and fall velocity of snowflakes between the two orthogonal cameras more accurately, provided the particle is correctly matched between the two view planes, and has been used to determine the scattering properties of snowflakes (Brandes et al. 2007; Huang et al. 2010, 2015; Bukovčić et al. 2018, 2020). The Multi-Angle Snowflake Camera (MASC) is another dedicated instrument designed to measure the properties of falling snowflakes. It captures high-resolution photographs of hydrometeors from three angles from which the habit can be identified (Garrett et al. 2012).

Corresponding author: Ali Tokay, tokay@umbc.edu

DOI: 10.1175/JTECH-D-20-0216.1

© 2022 American Meteorological Society. For information regarding reuse of this content and general copyright information, consult the AMS Copyright Policy (www.ametsoc.org/PUBSReuseLicenses).

The Precipitation Imaging Package (PIP), formerly called the Snow Video Imager (SVI) was developed to measure the size and fall velocity of snowflakes. It has been widely used since its introduction (Newman et al. 2009) and underwent several hardware and software upgrades by the instrument inventor, Dr. Larry F. Bliven of NASA Wallops Flight Facility (Pettersen et al. 2020a,b). Most of the studies used PIP observations to investigate the microphysical properties of falling snow (Tiira et al. 2016; Moisseev et al. 2017; von Lerber et al. 2017; Pettersen et al. 2020a,b; Kulie et al. 2021) and to simulate the retrieval of snow properties from dual- (Li et al. 2018) and triple-frequency radars (Kneifel et al. 2015; Falconi et al. 2018; Tyynelä and von Lerber 2019; Li et al. 2020) including GPM's Dual-Frequency Precipitation Radar (DPR) (Liao et al. 2016). Additionally, Pettersen et al. (2020b) demonstrated that the PIP-based bulk liquid water equivalent was within 2.5% agreement when compared to the collocated snow stake field over many events. Chase et al. (2020) used the PIP observations to examine the precipitation rate (PR)–melted mass-weighted mean diameter (D_{mass^*}) relationship in the presence of snow in the DPR algorithm and found out that the DPR power-law PR (D_{mass^*}) relationship is not optimal for snow. Measurement uncertainties of the SVI and PIP were evaluated by Wood et al. (2013) and Souverijns et al. (2017), respectively.

Of particular interest, Wood et al. (2014, 2015, W1415 hereafter) and von Lerber et al. (2017, 2018, vL1718 hereafter) described the methodology to retrieve the bulk snowfall characteristics including the snow water equivalent rate (SWER) and radar reflectivity (Ze) and used PIP measurements to test their retrieval processes. Pettersen et al. (2020b) compared the W1415 and vL1718 based bulk snowfall characteristics for low and high snow-to-liquid ratio events separately. The PIP measurements were used for this comparative study and a good agreement was found between the two retrieval methodologies. Pettersen et al. (2020b) found out that the W1415 and vL1718 retrieved SWER compared well to the independent PIP produced values of SWER.

This study uses PIP measurements to calculate the bulk descriptors of falling snowfall, snowfall rate (SR), and SWER. It should be noted that the SR refers to the snow intensity without melting while the SWER is the intensity of the melted equivalent of snow. The SR and SWER and their integral quantities snow depth (DP) and snow water equivalent (SWE) are the components of the climate record and have a wide range of applications in atmospheric and hydrological sciences. Among those, SWE are used for the short (\leq daily) and long-term global precipitation mapping, respectively. The measurements of SWE are collected by operational gauges at daily or higher time resolutions and these observations are often integrated with the remote sensing precipitation estimate such as the one done by Multi-Radar Multi-Sensor (MRMS) product (Zhang et al. 2016). The MRMS is a ground validation product for the GPM mission (Kirstetter et al. 2015). It has a rain–snow discrimination algorithm based on surface air and wet-bulb temperatures (Chen et al. 2016) and relies on a power-law relationship between Ze and SWER for snow.

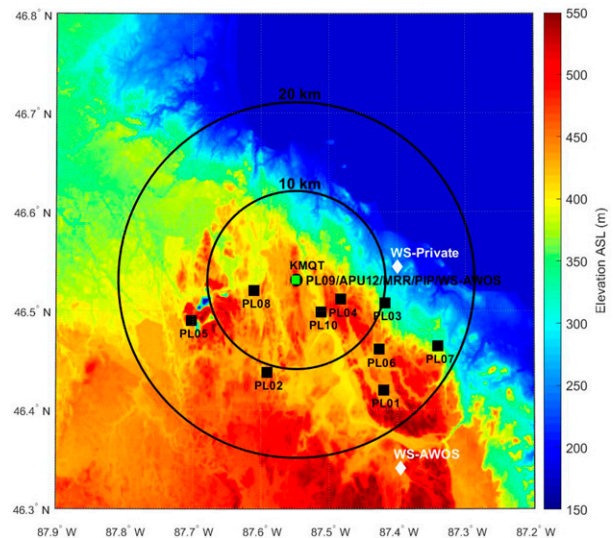


FIG. 1. Marquette (MQT) snowfall observatory data acquisition network. The master site includes the Precipitation Imaging Package (PIP), Pluvio² 200 weighing bucket gauge (PL09), complete weather station (WS) and NWS stake field, Micro Rain Radar (MRR), and Autonomous PARSIVEL² disdrometer Unit (APU). The NWS-Marquette radar site (KMOT) with 10- and 20-km ranges, nine Pluvio² 200/400 gauge sites, and NWS Sawyer Airport and private weather station sites are also shown.

This study evaluates the retrieved SWE from PIP observations through comparisons with a National Weather Service (NWS) reference observations (hereafter referred to as “snow stake field” measurements). It should be noted that the estimated SWE is referred as PIP-retrieved SWE for the rest of the paper. The measurement site, at Marquette, Michigan (MQT), and the instrumentation including PIP and precipitation gauges are summarized in section 2. Section 3 is devoted to retrieval methodology while the snow events that were determined based on PIP observations are listed in section 4. Section 5 compares collocated gauges and the catch efficiency of the gauges under windy conditions. The results of this study can be found in sections 6 and 7 for the detailed discussion of the two events and overall comparisons, respectively, followed by conclusions in section 8.

2. Measurement site and instrumentation

a. Measurement site

The GPM Field Support Office augmented the existing precipitation observing site at MQT by deploying 10 OTT Pluvio² 200/400 weighing bucket gauges and an Autonomous PARSIVEL² Unit (APU) at the beginning of December 2017. The master site (46.53°N, 87.55°W) adjacent to the NWS office is approximately 230 m above the nearby Lake Superior shoreline (Fig. 1) and has been equipped with a PIP and a K-band vertically pointing Micro Rain Radar (MRR) since January 2014 (Kulie et al. 2021; Pettersen et al. 2020a,b). The MRR provides the vertical structure of Ze and

TABLE 1. The list of the snow events. The columns are the event identification number, event date, event start and end day of year (DOY) and hour (HHHH) in UTC, number of snow minutes, PIP snow depth, and median, minimum, and maximum values of wet-bulb temperature and wind speed.

Event ID	Event date	Start (DOY: HHHH UTC)	End (DOY: HHHH)	Duration (min)	PIP DP (mm)	Wet-bulb temperature (°C): median, min, max	Wind speed (m s ⁻¹): median, min, max
1	6–7 Dec 2017	340: 1100	341: 1400	916	36.25	−9.1, −10.6, −8.1	5.1, 1.8, 8.5
2	8–10 Dec 2017	342: 0100	344: 0000	1434	84.23	−9.7, −12.3, −8.0	2.9, 0.4, 6.2
3	10–11 Dec 2017	344: 1400	345: 0100	410	21.03	−9.8, −11.7, −7.6	3.0, 1.3, 4.9
4	11–13 Dec 2017	345: 1300	347: 0000	1479	91.81	−11.3, −14.2, −5.6	4.2, 1.8, 8.0
5	13–16 Dec 2017	347: 1100	350: 0200	1976	122.54	−10.5, −13.9, −8.4	2.4, 0.4, 4.5
6	16 Dec 2017	350: 1100	350: 1400	92	4.68	−16.1, −20.0, −21.6	0.9, 0.4, 1.3
7	17–18 Dec 2017	351: 1100	352: 0400	193	3.83	−4.5, −4.8, −4.3	2.5, 1.8, 3.6
8	19–22 Dec 2017	353: 0100	356: 0000	1611	60.65	−6.4, −11.2, 0.0	3.6, 0.4, 10.7
9	23 Dec 2017	357: 0700	357: 2200	360	10.23	−9.9, −11.3, −8.3	3.7, 1.8, 6.7
10	28–29 Dec 2017	362: 1800	363: 1000	650	5.16	−16.4, −19.2, −14.5	1.7, 0.4, 3.1
11	3–6 Jan 2018	003: 1300	006: 1500	3765	104.29	−17.0, −19.1, −12.7	3.5, 1.8, 6.7
12	7 Jan 2018	007: 0700	007: 1500	170	4.59	−13.2, −14.9, −10.9	4.9, 3.1, 7.1
13	11–12 Jan 2018	011: 1800	012: 2200	1446	77.13	−12.4, −17.0, 0.5	4.8, 0.4, 5.4
14	15–16 Jan 2018	015: 0200	016: 2300	2070	159.87	−10.2, −14.4, −7.1	1.7, 0.4, 5.4
15	22–23 Jan 2018	022: 0800	023: 2300	1326	239.17	−5.2, −9.9, −2.4	3.9, 1.3, 6.7
16	31 Jan 2018	031: 0100	031: 1400	270	27.27	−7.2, −11.0, −5.8	4.8, 3.1, 8.9
17	1–2 Feb 2018	032: 0500	033: 0000	495	8.42	−16.4, 18.5, 10.3	5.3, 3.1, 8.5
18	3–4 Feb 2018	034: 0100	035: 1000	1146	25.95	−15.2, −17.5, −12.4	2.1, 0.4, 5.3
19	19–20 Feb 2018	050: 1500	051: 1800	828	50.99	−7.1, −8.2, −6.0	3.5, 1.8, 5.3
20	24 Feb 2018	054: 0500	054: 1500	410	67.50	−5.0, −5.5, −3.1	1.2, 0.4, 3.1
21	26 Feb 2018	056: 0400	056: 1800	363	70.77	−3.0, −4.4, −1.9	4.9, 1.3, 11.2
22	28 Feb 2018	059: 0500	059: 0800	124	19.48	−1.7, −2.3, −1.1	0.4, 0.4, 0.9
23	6–7 Mar 2018	065: 1800	066: 2300	1588	231.87	−7.6, −9.4, −4.7	3.2, 1.3, 5.8
24	12–14 Mar 2018	071: 0100	073: 0000	1485	99.04	−5.7, −9.6, −2.1	3.6, 0.4, 6.2
25	30–31 Mar 2018	089: 1700	090: 1700	805	105.29	−6.7, −8.4, −4.4	1.4, 0.4, 3.6
26	1 Apr 2018	091: 0600	091: 1200	270	14.47	−11.9, −14.7, −11.2	1.7, 0.9, 2.7
27	4 Apr 2018	094: 0200	094: 1300	358	12.43	−7.5, −8.3, −6.8	3.9, 2.2, 6.2
28	5–6 Apr 2018	095: 0800	096: 2100	431	21.17	−6.5, −11.3, −2.7	3.5, 0.4, 8.9
29	12 Apr 2018	102: 0800	102: 1600	424	110.66	−1.2, −2.0, 1.3	0.9, 0.4, 2.7
30	15–18 Apr 2018	105: 1000	108: 0000	3045	455.00	−5.6, −7.2, −3.3	4.8, 1.8, 8.5

Doppler velocity (W) at 100-m gate spacing within 3 km above the ground. The daily PIP and MRR observations are posted online at https://www.ssec.wisc.edu/lake_effect/mqtl/. The NWS office also operates a complete weather station and a manual snow stake field at the master site. Weather station and snow field observation details can be found in [Pettersen et al. \(2020a\)](#). The NWS Marquette Weather Surveillance Radar (KMQT) is located 80 m from the master site. The Pluvio² gauges were distributed up to 17 km from KMQT and one of the Pluvio² 200 gauges (PL09) and APU are collocated with the other instrumentation at the master site.

b. PIP

PIP records the two-dimensional grayscale video images (see Figs. 6 and 10, [Kneifel et al. 2015](#)) of falling particles between a light source and a high-speed camera that are 2 m apart. The field of view (FOV) is calculated based on the 48 mm × 64 mm calibration image considering edge effects. The focal plane is about 1.3 m from the lenses and the depth of field (DOF) is size dependent. The sampling volume is a

multiplication of FOV, DOF, and the number of frames over a given time period. Considering a single particle with 1 mm in equivalent diameter (D_{eq}), the sampling volume is 3.95 m³ for a 1-min observation period. This is relatively larger than the corresponding sampling volumes of 2DVD and PARSIVEL², 2.40 and 1.25 m³, respectively.

The PIP's pixel size is 0.1 mm × 0.1 mm and the particles with less than 14 pixels are rejected. This effectively rejects the particles $D_{eq} < 0.2$ mm. The standard sizing error for the SVI was reported as approximately 18% ([Newman et al. 2009](#)) and the current setup uses half of DOF reducing the uncertainty in the size measurements. The use of a higher speed camera enabled with particle tracking software allows the PIP to measure the fall velocity of individual particles ([Pettersen et al. 2020b](#)). This is one of the major improvements of the PIP from its original version, SVI. Depending on the direction of the particle entering and leaving the sample volume and particle size, particles have been photographed multiple times, which provide a unique information regarding the particle's motion. The PIP's measurement volume is not

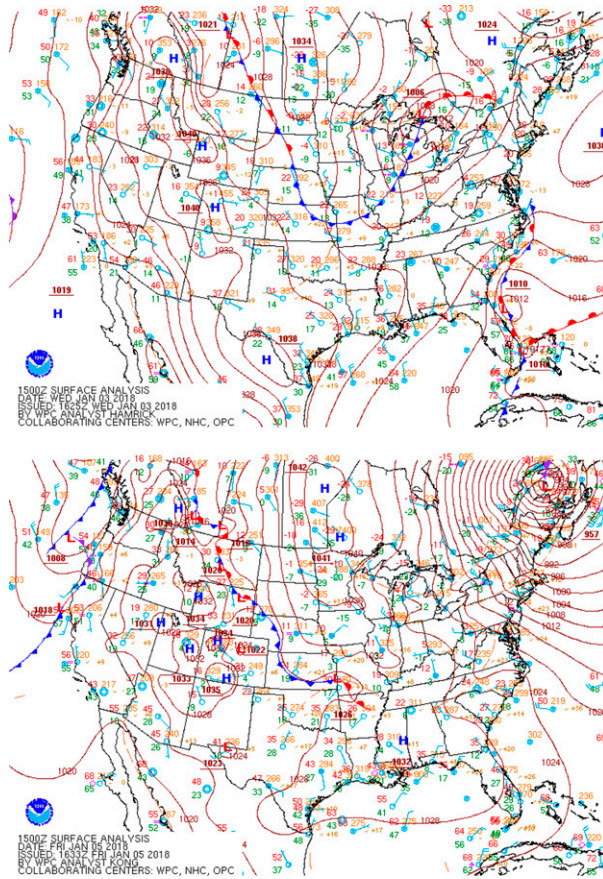


FIG. 2. The NWS surface analysis for (top) 1500 UTC 3 Jan and (bottom) 1500 UTC 5 Jan 2018.

enclosed, and therefore, it is immune to the secondary particles due to splashing and undersampling in windy conditions. This is one of the advantages of PIP with respect to the 2DVD and PARSIVEL.

The PIP's raw data have been grouped under particle, track, and velocity files. The record number and time stamp are included in each file that covers a 10-min time span. The particle file was generated following National Instruments Image Acquisition (IMAQ) software and outputs selected variables listed in Table 10-1 of IMAQ vision concepts manual (National Instruments 2004). The definitions of the various descriptors of the size parameters including D_{eq} and maximum dimension of the particle (D_{mx}) are given in the appendix. It should be noted that D_{eq} and D_{mx} are key for the retrieval assumptions and Fig. 1b of von Lerber et al. (2017) shows the schematic image of plane projection of the side view of PIP snowflake with D_{eq} and D_{mx} .

The track files include, particle identification, record number, and D_{eq} but do not include other descriptors of size parameters that can be found in particle file. A lookup table is generated where the record numbers are grouped by the particle identification number. Interestingly, a few particles had more than 20 records with a maximum of 59 records in our dataset. The user needs to combine particle and track files to

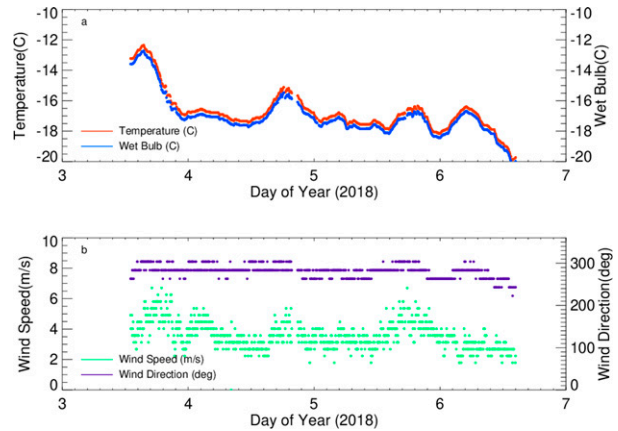


FIG. 3. Time series of (a) air temperature and wet-bulb temperature and (b) wind direction and speed observations from the weather station at the master site for event 11.

determine the mean and maximum values of particle dimensions.

There are two velocity files. One is dedicated for the particles observed twice and the other is for the particles observed more than twice. The velocity files include the particle identification number from which the particle is matched, and the mean fall velocity is calculated. It is feasible that the particle may have negative (upward) fall velocity. Particles less than 0.5 m s^{-1} are excluded from the analysis (von Lerber et al. 2017).

The PIP also produces the higher-order products including estimates of effective density and precipitation rate as detailed in Pettersen et al. (2020b). The effective density is critical for the PIP derived SWER, which is used for a comparative study with W1415 and vL1718 retrieved SWE. Lee and Chandrasekar (2019), on the other hand, presented rain rate (RR) and SWER time series to demonstrate the mixed phase period as a validation tool for the precipitation phase algorithm.

c. Precipitation gauges

The OTT Pluvio² 200 is a heated weighing bucket gauge with a 200-cm^2 orifice. It outputs real-time and non-real-time precipitation totals at 0.01-mm resolution for a predetermined sampling interval, which is typically 1 min. The non-real-time precipitation accumulation has a 5-min delay and is reliable for 10-min or longer observation periods.

The NWS snow stake field features an overflow can, collector funnel, and measuring tube and has a 324-cm^2 orifice. When solid precipitation is expected, the collector funnel and measuring tube are removed and the snow is accumulated to the overflow can. The snowfall in the overflow can is first melted and then poured in the measurement tube. The water content corresponds to the nearest 0.01 inch (0.254 mm) reading in the measurement tube. The measurement is taken every 6 h at 0000, 0600, 1200, and 1800 UTC and at local midnight (0500 UTC). Snow board totals are also recorded

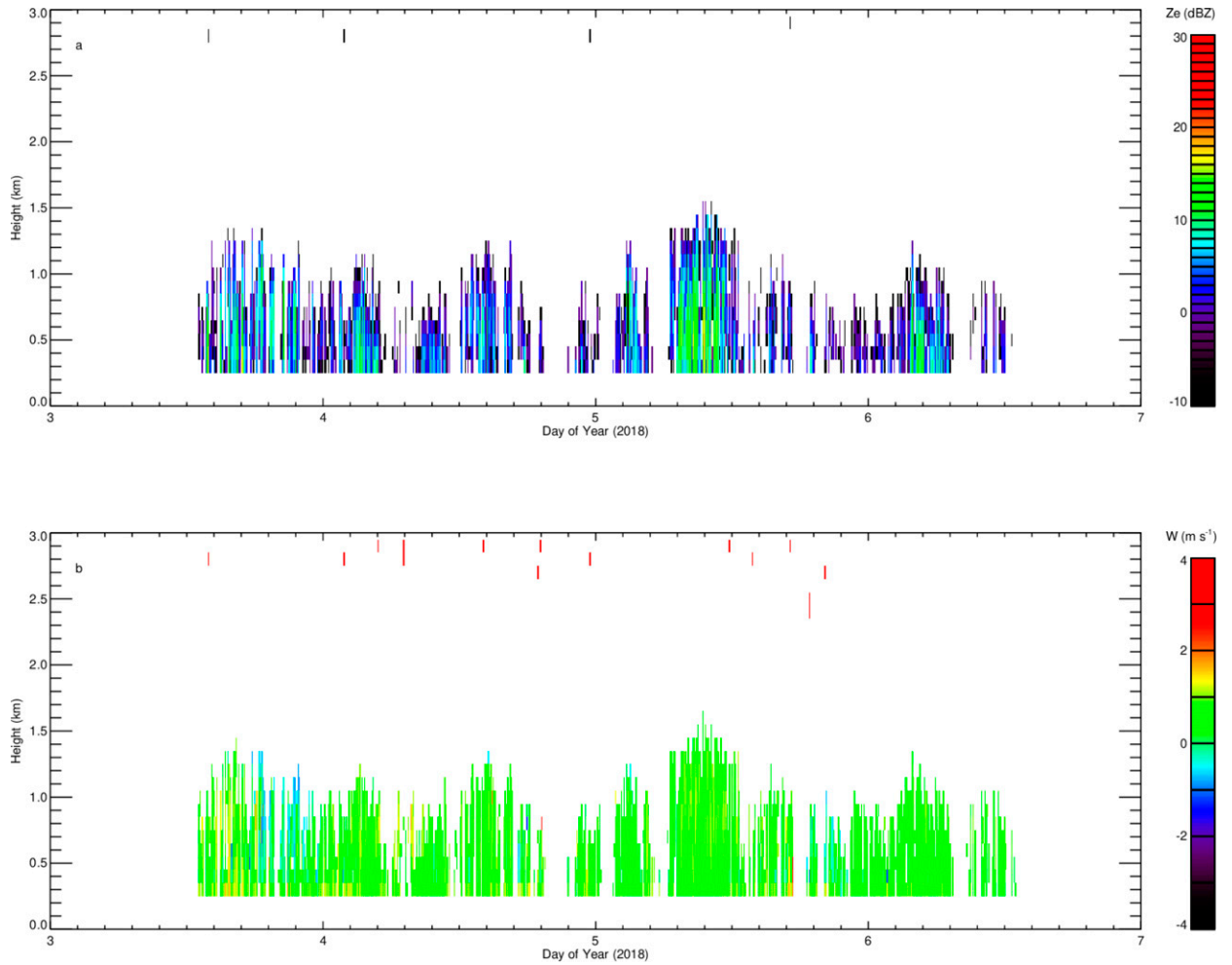


FIG. 4. Times series of (a) equivalent reflectivity (Z_e) and (b) Doppler velocity (W) from Micro Rain Radar at the master site for event 11.

at the same measurement cadence. The local NWS offices in the northern United States (e.g., MQT office) often map the annual totals of winter precipitation under their jurisdiction.

Both the OTT Pluvio² 200 and stake field have single Alter shields but this may not be sufficient in windy conditions (Rasmussen et al. 2012). The double fence intercomparison reference (DFIR) is considered as a standard for the snow measurements (Yang 2014). Kochendorfer et al. (2017) offered the catchment efficiency transfer function (CETF) for unshielded and single-Alter-shielded gauges when the weather station is at the gauge height and on a 10 m tower. This study uses the following form of CETF:

$$\text{CETF} = \exp\{-aU[1 - \tan^{-1}(bT_{\text{air}} + c)]\}, \quad (1)$$

where U and T are the 30-min averages of wind speed (m s^{-1}) and air temperature ($^{\circ}\text{C}$), respectively. The coefficients a , b , and c are 0.0348, 1.366, and 0.779, respectively. They are chosen based on the presence of an Alter-shield gauge and a

weather station at the gauge height. Equation (1) is valid when the mean wind speed is less than 7.2 m s^{-1} and this was the case for all the events used in this study.

The CETF was applied to the Pluvio² gauge whenever the gauge recorded precipitation. The mean wind speed and temperature were calculated from the data collected within ± 15 min of the gauge measurement time. Snow stake field observations were manipulated to mimic the Pluvio² gauge time stamps. A time series of the PIP SR is a reliable source for the intensity change at 1-min resolution. For the NWS snow measurement observational period (1 or 6 h since midnight falls in 0500 UTC during EST), a calibration constant was determined by taking the ratio of the stake field total to the PIP DP. The calibration constant was then multiplied with the PIP SR and the SR was accumulated from the beginning of the stake field observation period. Once the accumulation reached 0.01 mm, the time stamp (e.g., min) was saved and the accumulation was reset to zero. One-minute accumulations were as high as 0.13-mm accumulation in this study. The CETF was then applied to the manipulated stake field observations.

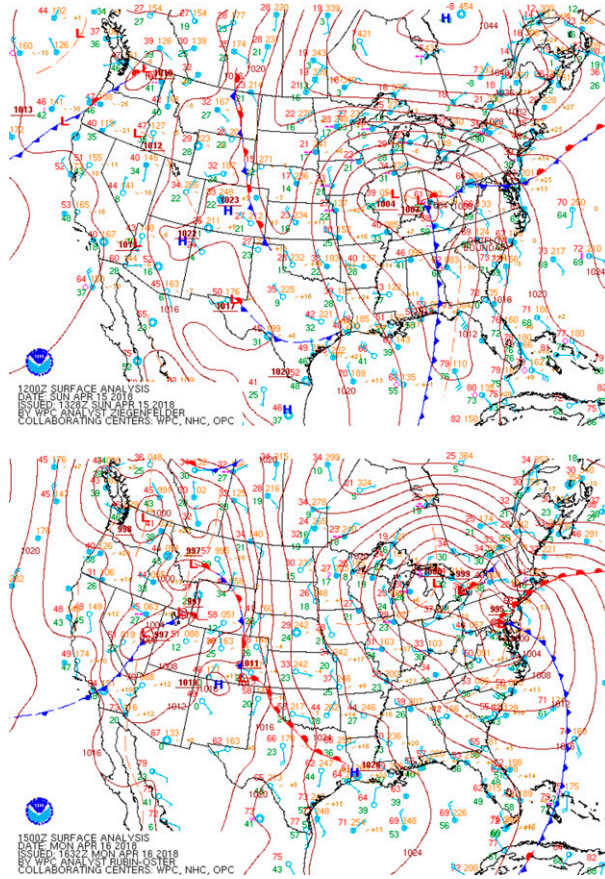


FIG. 5. The NWS surface analysis for (top) 1200 UTC 15 Apr and (bottom) 1500 UTC 16 Apr 2018.

3. Retrieval methodology

This section describes the DP and SWE calculation procedure from PIP particle size and velocity measurements. The accuracy of PIP measurements including particle concentration, the choice of prescribed $D_{mx}-D_{eq}$ relationships, and four different approaches of particle mass calculation play an important role in determining the SWE.

a. SSD

The snowflake size distribution (SSD) is the number of particles in a volume of air in the i th size interval, $N(D_{eq,i})$ and is expressed as a function of DOF and FOV, both of which vary with the particle size. It is formulated as

$$N(D_{eq,i}) = \frac{1}{TN_f \Delta D_{eq,i}} \sum_{j=1}^N \frac{1}{DOF_{i,j} FOV_{i,j}}, \quad (2)$$

where T is the period of observation (typically 60 s); N is the number of particles in i th size bin; N_f is the number of frames (380 frames per second), which is substantially higher than SVI (the fewer than 60 frames per second; Newman et al. 2009); ΔD_{eq} is the particle bin width which is set to 0.2 mm;

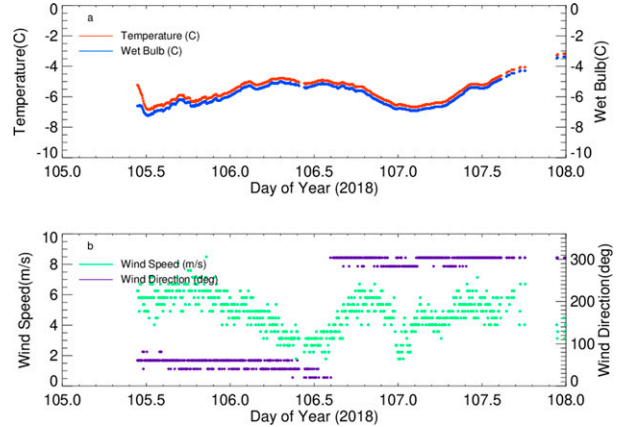


FIG. 6. Time series of (a) air temperature and wet bulb and (b) wind direction and speed observations from the weather station at the master site for event 30.

$FOV (m^2) = 10^{-6} (48 - D_{eq})(64 - D_{eq})$; and $DOF (m) = (0.117/2)D_{eq}$, where D_{eq} is in millimeters.

Time series of size distribution are useful for characterizing the precipitation systems with different origins. In rain, the presence of an abundance of small drops in tropical cyclones and their absence in extratropical cyclones was shown in a study in mid-Atlantic region (Tokay et al. 2008). In snow, the shallow lake-effect events had fewer small particles than the deep synoptic events (Pettersen et al. 2020a). For rain, the +small, midsize, and large drops are separated with size thresholds of 1 and 3 mm such that the drops larger than 3 mm in diameter are considered as large (Tokay et al. 2014). For snow, the size threshold between the midsize and large flakes is considered as 5 mm in diameter since both aggregates and graupel often reach sizes above this threshold. Hence, the midsize flakes are considered between 1 and 5 mm in diameter in this study.

b. Snowflake mass

The mass of a snowflake (m) has been expressed as a function of D_{mx} . Matrosov (2007) relied on horizontally oriented dry aggregate measurements of Magono and Nakamura (1965) in Japan and offered the following expressions for the mass of a snowflake in grams for a wide range of D_{mx} of a spheroid (mm):

$$m = \begin{cases} 3.0 \times 10^{-5} D_{mx}^{2.0} & (0.1 < D_{mx} \leq 2 \text{ mm}) \\ 2.1 \times 10^{-5} D_{mx}^{2.5} & (2 < D_{mx} \leq 20 \text{ mm}) \\ 4.7 \times 10^{-5} D_{mx}^{3.0} & (D_{mx} > 20 \text{ mm}) \end{cases} \quad (3)$$

While this set of $m-D_{mx}$ relationships have been used for the backscattering cross section calculations (Leinonen et al. 2012), it was recognized that $m-D_{mx}$ relationship has a wider range due to the particle habit which diverges from a dry spheroid (Tyynelä and Chandrasekar 2014). Tiira et al. (2016) suggested $m = 6.4 \times 10^{-5} D_{mx}^{2.002}$ and $m = 4.9 \times 10^{-5} D_{mx}^{2.031}$ relationships based on PIP measurements for two consecutive winters in Finland where the former winter has more rimed particle in milder conditions. For a particle where $D_{mx} = 3$ mm,

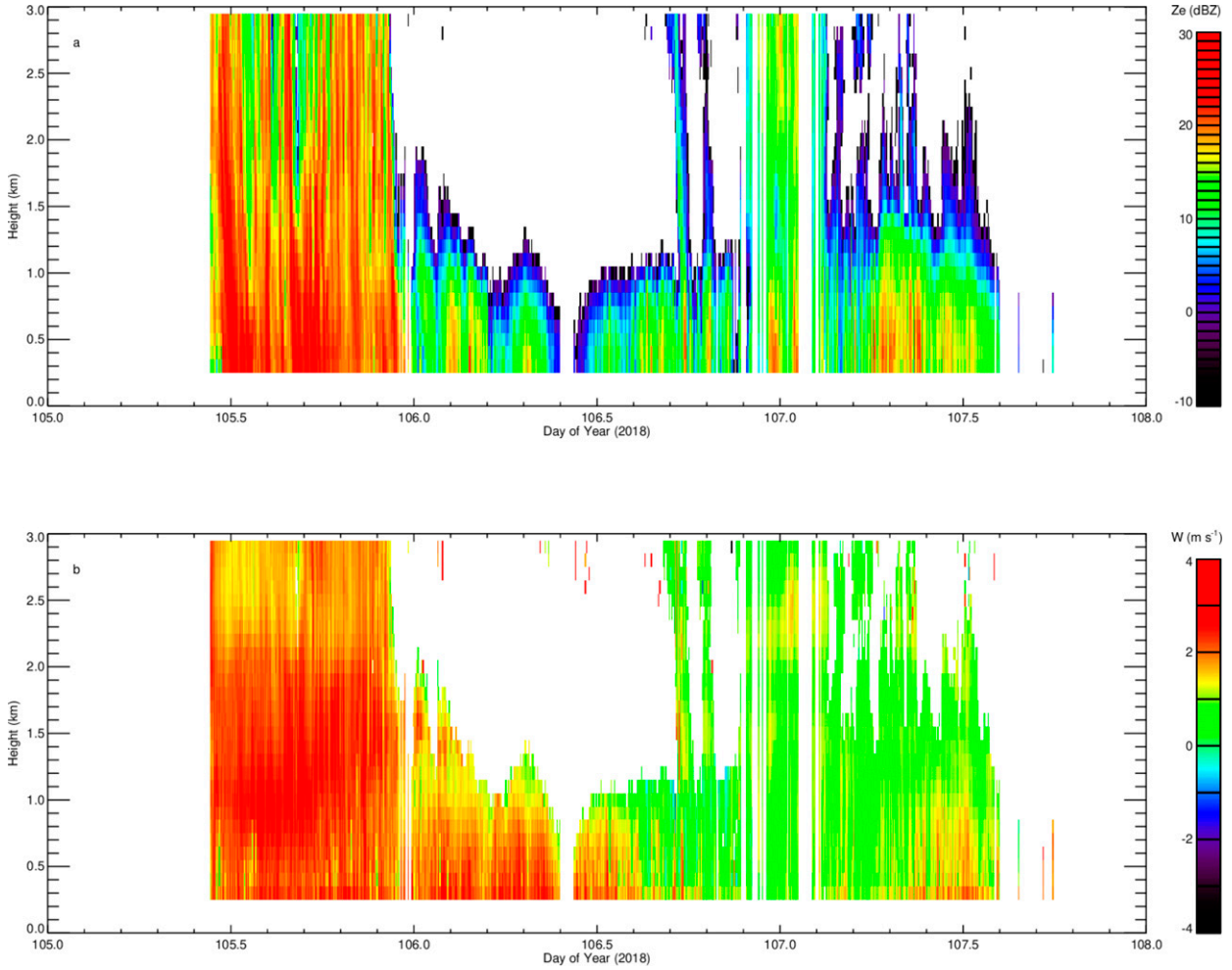


FIG. 7. Times series of (a) equivalent reflectivity (Z_e) and (b) Doppler velocity (W) from Micro Rain Radar at the master site for event 30.

snowflake mass is 23% higher during the first winter than the second and is between the two winters if Eq. (6) is used.

This study recognizes the dependency of the particle mass on the habit and uses the hydrometeor aerodynamics outlined by Böhm (1989, BM hereafter). A similar approach was used by Szyrmer and Zawadzki (2010, SZ hereafter) and von Lerber et al. (2017) and the process used in this study is explained in the following four steps.

First, the PIP D_{mx} is prescribed as a function of D_{eq} as follows:

$$D_{mx} = \alpha D_{eq}, \quad (4)$$

where $\alpha = 1.2, 1.3, 1.4$, and 1.5 . Using PIP measurements, von Lerber et al. (2018) reported α between 1.28 and 1.49. Assuming spheroidal shape with axis ratio of 0.6 (Li et al. 2018), Moiseev et al. (2017) found α to be 1.25. PIP fall velocity measurements are binned as a function of D_{mx} at 5-min intervals (von Lerber et al. 2017). The bin width is set to 0.2 mm and the midsize diameter of the bin ranges from 0.1 to 19.9 mm. The fall velocity measurements within a bin did not necessarily follow a normal distribution, mainly due to outliers at the high end as previously observed in Tiira et al. (2016).

Here the median rather than mean fall velocity (v) is therefore represented in each bin.

Second, the Reynolds number (Re) was calculated from the median fall velocity for each size bin using the midsize diameter and is expressed as

$$Re = v D_{mx} \rho_a / \eta, \quad (5)$$

where ρ_a and η are the density of air and dynamic viscosity, respectively, and are calculated from environmental variables extracted from the weather station observations at the MQT NWS site.

Third, the Best number (X) is calculated from Re for each size bin and is expressed as

$$X = \left(\frac{\delta_0^2 C_0^{1/2}}{4} \left\{ \left[\frac{(4Re)^{1/2}}{\delta_0} + 1 \right]^2 - 1 \right\} \right)^2, \quad (6)$$

where δ_0 , and C_0 are the boundary layer thickness and the drag coefficient and are taken as 5.83 and 0.6, respectively, following BM. Equation (6) is a generalized theoretical

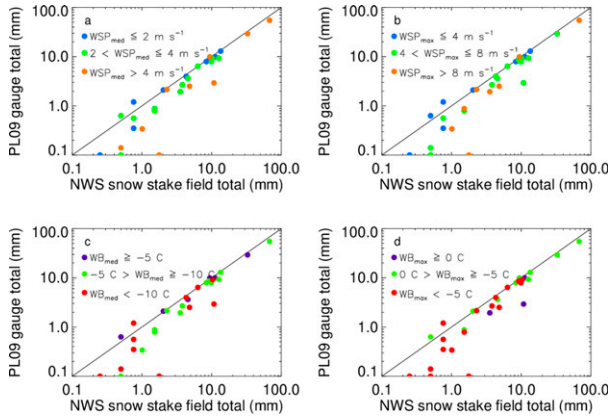


FIG. 8. Comparison of Pluvio² 200 weighing bucket gauge (PL09) and NWS stake field snow water equivalent event totals as a function of (a) median wind speed (WSP), (b) maximum wind speed, (c) median wet-bulb (WB) temperature, and (d) maximum wet-bulb temperature.

relationship between Re and X considering an idealized spheroidal snowflake shapes. Mitchell and Heymsfield (2005, MH hereafter) expressed Re as a function of the X , reversing Eq. (9) and added an empirical term $-a_0 X_0^b$ where $a_0 = 0.0017$ and $b_0 = 0.8$ for a turbulence correction to increase the drag at very large Re in the presence of large aggregates. Khvorostyanov and Curry (2005, KC hereafter) offered an alternative approach for the turbulence drag. Both MH and KC aimed to achieve more realistic particle fall velocities. SZ reformulated the MH and KC X - Re relationships with an eight-order polynomial where $\log(X)$ is expressed as a function of $\log(Re)$:

$$\log(X) = \sum_{l=1}^8 C_l [\log(Re)]^l, \quad (7)$$

where $C_1 = C_{MH,1}$ for the MH X - Re relation and $C_1 = C_{KC,1}$ for the KC X - Re relation. The coefficients of $C_{MH,1}$ and $C_{KC,1}$ are given in Table 2 of the SZ study and are used as an second and third alternative X in this study. Heymsfield and Westbrook (2010, HW hereafter) sought a better agreement between the observed and theoretical fall velocities in the presence of pristine ice crystals and aggregates. They suggested $\delta_0 = 8.0$ and $C_0 = 0.35$ in Eq. (6) and this has been employed as a fourth alternative X in this study.

Fourth, the mass of a snowflake was calculated from the X for each size bin and is expressed as

$$m = \frac{\pi \eta^2 X}{8g\rho_a} \left(\frac{A_e}{A} \right)^t, \quad (8)$$

where g is the gravitational constant, A_e is the effective particle area, and A is the area of the smallest circle or ellipse which contains A_e . The area ratio (A_e/A) is also explained as $(D_{eq}/D_{mx})^2$ and is 0.69, 0.59, 0.51, and 0.44

for $\alpha = 1.2, 1.3, 1.4$, and 1.5 , respectively. The exponent t is equal to 0.25 for BM, MH, and KC methods, and is 0.5 for HW method.

Power-law fits were applied to v - D_{mx} and m - D_{mx} relationships using orthogonal least squares and are expressed as

$$v = a_v D_{mx}^{b_v}, \quad (9a)$$

$$m = a_m D_{mx}^{b_m}. \quad (9b)$$

The fitting was based on the median values of fall velocity ($m\ s^{-1}$) and mass (g) in each size bin and bin midsize D_{mx} (cm). Each size bin should have at least 10 snowflakes to calculate the median values of velocity and mass and this condition should be satisfied for at least eight size bins; otherwise, the fitting was not applied.

c. Snow depth

The DP is a geometric depth of falling snow for a period of observation. It is expressed as functions of particle volume, concentration, and fall velocity and is given in units of millimeters for 60 s (dt) of observation:

$$DP = \pi 10^{-5} \int_t^{t+\Delta t} \int_{D_{min}}^{D_{max}} v(D_{mx}, t) D_{eq}^3 N(D_{eq}, t) dD_{eq} dt. \quad (10)$$

The particle fall velocity in Eq. (10) is a function of D_{mx} and the DP are therefore calculated for the four values of α in the D_{mx} - D_{eq} relationship. The NWS measures the geometric depth using a snow board that is cleared after every measurement interval. The main difference between the NWS measurement and geometric depth derived from Eq. (10) is the packing efficiency of the snowflakes and the snow compression. Tiira et al. (2016) pointed out the packing efficiency as 70% for the worst case scenario and the snow compression close to unity for a freshly fallen snow. These two factors should be considered if the DP is compared to the NWS measurement which is beyond the scope of this study.

d. Snow water equivalent

The SWE is an accumulation of liquid equivalent of falling snow. It is expressed as functions of mass, fall speed, and concentration of the particles in a volume of air and is in units of millimeters for 60 s (dt) of observation:

$$SWE = \frac{6 \times 10^{-2}}{\rho_w} \int_t^{t+\Delta t} \int_{D_{min}}^{D_{max}} m(D_{mx}, t) v(D_{mx}, t) N(D_{eq}, t) dD_{eq} dt, \quad (11)$$

where ρ_w is the density of water ($g\ cm^{-3}$).

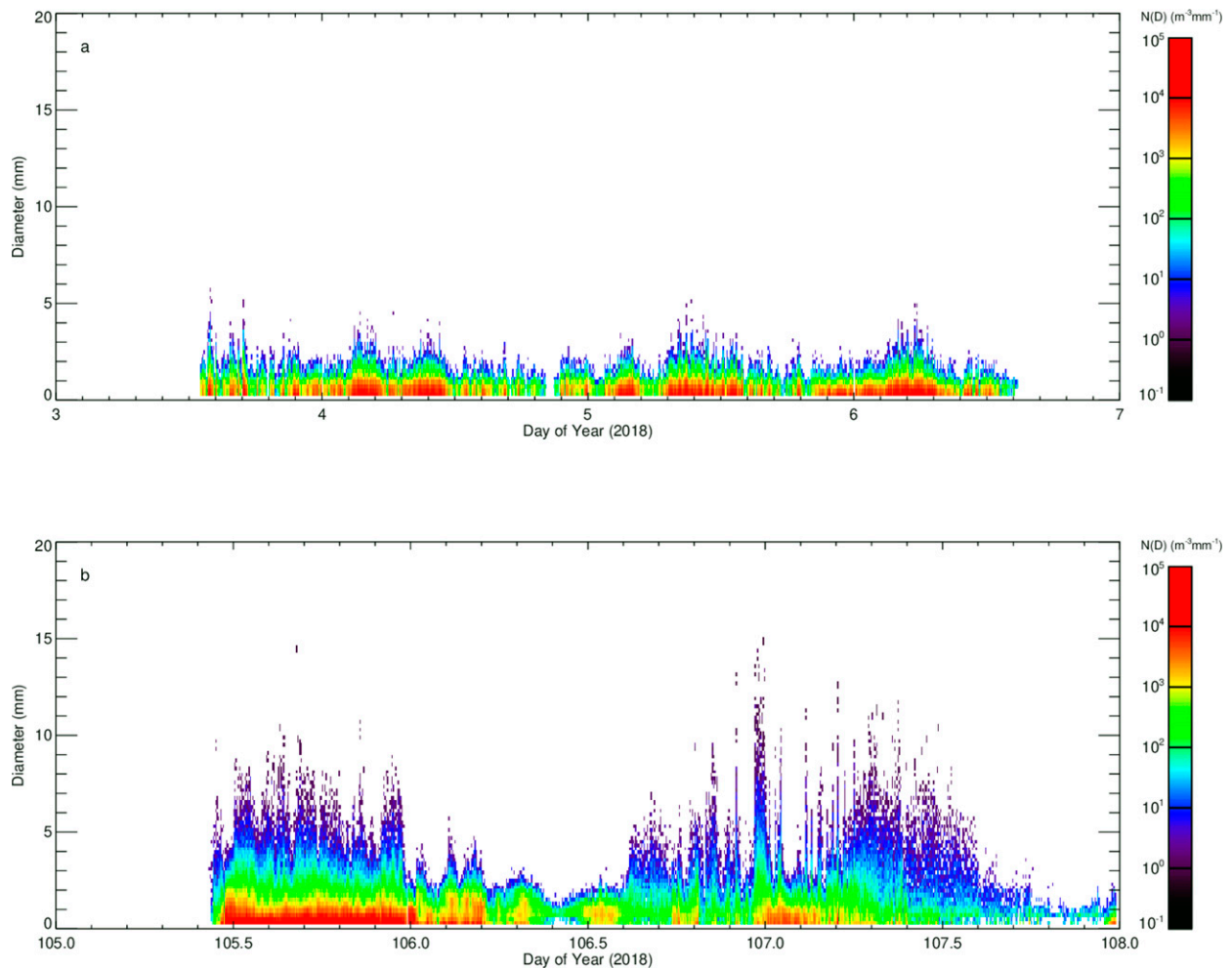


FIG. 9. Time series of snowflake size distribution for (a) event 11 and (b) event 30.

4. Snow events

The PIP SR time series were used to define the snow events. Precipitating periods were recognized when a minimum sample of 50 particles and a minimum intensity of 0.1 mm h^{-1} were observed over 1-min intervals. The collocated APU, which has a built-in algorithm for retrieving the precipitation phase (Yuter et al. 2006) and the wet-bulb temperature from collocated weather station were examined to determine periods with frozen precipitation. A total of 30 snow events were then identified based on following three conditions: 1) the time gap between the two consecutive events was longer than 12 h; 2) the DP was 3 mm or higher; 3) the event had at least 90 samples. Table 1 denotes the snow events with the event number, event date, start and end day of year (DOY) and hour (HHHH) in UTC, total number of snowy minutes, PIP DP, and median, minimum, and maximum values of wet-bulb temperature and wind speed. During the 2017/18 winter, PIP accumulated 2345.8 mm of geometric DP in 499 h. Event 11 was the longest, while event 30 had the highest accumulation. These two events are different in many aspects and this

study uses these two events as representation of the two predominant snowfall regimes at MQT (see also Pettersen et al. 2020a,b; Kulie et al. 2021).

Event 11 had 3 days and 2 h of nearly continuous lake-effect snowfall. The storm started when a low pressure center was situated between Lake Superior and Lake Huron with a north-south elongated cold front and west-east arc shape warm front at 1500 UTC 3 January 2018 (Fig. 2a). This is a classical extratropical cyclone scenario frequently observed in upper Midwest in winter. The low pressure center moved northeast and a high pressure center penetrated to south, centering on southwest Ontario, Canada, at 1500 UTC 5 January 2018 (Fig. 2b); a perfect configuration for the northwesterly flow fetching from Lake Superior to MQT shore. The wet-bulb temperature ranged between -16° and -18°C for most of the event (Fig. 3a). The winds were moderate with a median wind speed of 3.5 m s^{-1} and blew from northwest for the entire event (Fig. 3b). Time series of the MRR Ze and W showed echo tops less 1.5 km with $\text{Ze} \leq 15 \text{ dBZ}$ (Fig. 4a) and $W \leq 1 \text{ m s}^{-1}$ (Fig. 4b) for the entire event.

TABLE 2. The minimum, median, mean, and maximum values of total concentration (N_T), mass-weighted mean diameter (D_{mass}), maximum particle diameter (D_{max}), and the shape parameter of the gamma fitted distribution (μ) for events 11 (top value for each parameter) and 30 (bottom value).

SSD parameters	Minimum	Median	Mean	Maximum
N_T (m^{-3})	105 44	1932 1306	2705 3959	13 828 28 205
D_{mass} (mm)	0.63 0.80	0.92 2.18	0.96 2.61	2.47 9.86
D_{max} (mm)	0.90 1.10	1.90 3.90	1.95 4.25	4.70 12.90
μ	0.2 −2.2	2.8 1.1	3.1 1.4	9.8 20.0

Event 30 was an example of a spatially variable storm. The event can be divided into different segments depending on synoptic and microphysical analyses, respectively. The event started when a low pressure centered over Indiana with a north–south elongated cold front at 1200 UTC 15 April 2018 (Fig. 5a). MQT, located well within the cold sector, received northeasterly flow. The low pressure center moved to the mid-Atlantic and a secondary low formed over Lake Huron at 1500 UTC 16 April 2018 (Fig. 5b). The wet-bulb temperature ranged between -5° and -7°C for most of the event (Fig. 6a). The winds were moderate with a median wind speed of 4.8 m s^{-1} , while the wind direction shifted from northeast to northwest at around 1430 UTC April 16 (Fig. 6b). This coincided with the eastward movement of the low pressure system. Time series of MRR Ze and W exhibited three distinct segments of the storm. The first segment ending near 0000 UTC 16 April had radar echoes for the entire column with $\text{Ze} > 20 \text{ dBZ}$ (Fig. 7a) and $W \sim 2.5 \text{ m s}^{-1}$ (downward) near the ground (Fig. 7b). The second segment ending 1800 UTC April 16 was a shallow period with echo tops mostly less than 1.5 km with $\text{Ze} \leq 15 \text{ dBZ}$ and $W \sim 2.0\text{--}2.5 \text{ m s}^{-1}$. The third segment was a mixture of brief deep and shallow periods of snowfall with echo tops ranging between 1.5 and 3.0 km. The shallow MRR reflectivity features and microphysical evolution associated with the second and third segments of this event indicate likely lake and orographic enhancement processes that frequently occur at this site (Kulie et al. 2021). The MRR Ze was bounded mostly between 10 and 20 dBZ while MRR W gradually decreased from 2 to $<1 \text{ m s}^{-1}$ until the last gap in the time series at 0100 UTC 17 April and increased to over 2 m s^{-1} .

5. Gauge measurements

Gauges provide direct precipitation measurements and are therefore used as a reference for evaluating the performance of disdrometers (Tokay et al. 2013, 2014). Indeed, this study used the gauge measurements to evaluate the PIP derived SWE with caution. Ideally, multiple heated weighing bucket gauges are operated within double fence intercomparison reference, but this is only feasible for a study focusing on gauge accuracy in winter precipitation (Rasmussen et al. 2012).

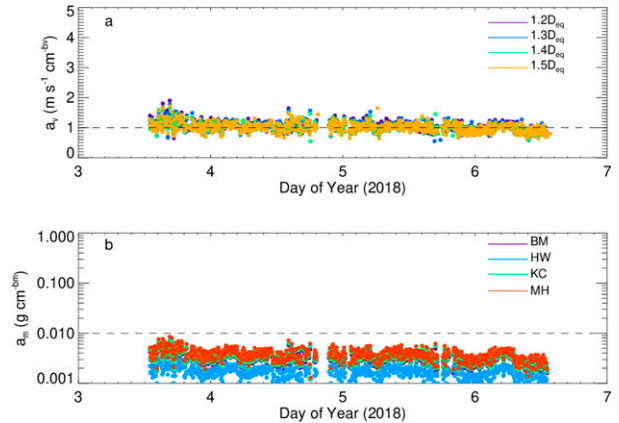


FIG. 10. Time series of (a) coefficient (a_v) of the v – D_{max} relationships for event 11 when PIP maximum particle dimension is equal to $1.2D_{\text{eq}}$, $1.3D_{\text{eq}}$, $1.4D_{\text{eq}}$, and $1.5D_{\text{eq}}$, (b) coefficient (a_m) of the m – D_{max} relationship for event 30 when PIP mass estimate is based on BM, HW, KC, and MH methods when $D_{\text{max}} = 1.4D_{\text{eq}}$.

The comparison of collocated PL09 and snow stake field measurements revealed that PL09 underestimated event totals nearly in all events (Fig. 8). This was partly due to the PL09 malfunction. Stake field errors are primarily due to coarse resolution of 0.01 in (1 in. = 25.4 mm). Two-thirds of the events in December 2017 had less than 2 mm SWE where the PL09 and stake field totals differed by more than 25%. Such large differences between the two measurements were also evident for the low SWE events observed in 2018. About 80% of the events in 2018 had SWE more than 2 mm where the differences between the two were less than 20% nearly in all events, indicating a reasonable agreement. The events with high median wind speed ($\text{WSP}_{\text{med}} > 4 \text{ m s}^{-1}$) or low median wet-bulb temperature ($\text{WB}_{\text{med}} < -10^{\circ}\text{C}$) did not necessarily have the large differences in precipitation totals (Fig. 8). This was also the case when the event maximum wind speed ($\text{WSP}_{\text{max}} > 8 \text{ m s}^{-1}$) or maximum wet-bulb temperature ($\text{WB}_{\text{max}} < -5^{\circ}\text{C}$) was considered.

6. Two predominant events

a. Snow size distribution

SSD time series between events 11 and 30 were significantly different (Fig. 9; see also Table 2). Event 11 had a relatively uniform distribution with abundant small flakes, low concentrations of midsize flakes and an absence of large flakes. The low concentrations of midsize flakes were mainly due to the lack of flakes between 3- and 5-mm size range (Fig. 9a). Event 30 showed intraevent variability reflecting the three segments observed in MRR Ze and W time series. The abundant small flakes, high concentration of midsize flakes, and the presence of large flakes between 5 and 10 mm in D_{eq} were the characteristic features of the first segment (Fig. 9b). The narrow size spectra, with maximum flake size less than 3 mm dominated the second segment. The concentration of small flakes was also less than the first segment particularly toward the end of

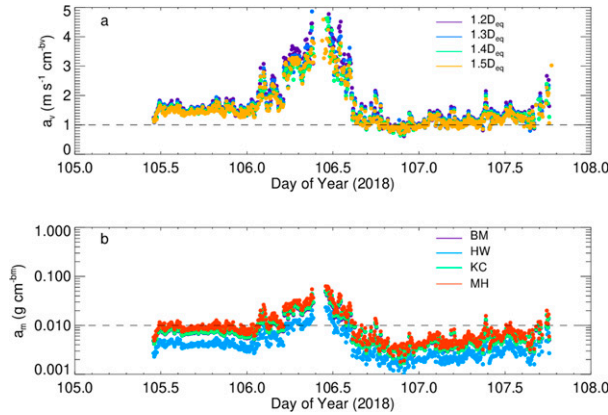


FIG. 11. Time series of (a) coefficient (a_v) of the v - D_{mx} relationships for event 30 when PIP maximum particle dimension is equal to $1.2D_{eq}$, $1.3D_{eq}$, $1.4D_{eq}$, and $1.5D_{eq}$, (b) coefficient (a_m) of the m - D_{mx} relationship for event 30 when PIP mass estimate is based on BM, HW, KC, and MH methods when $D_{mx} = 1.4D_{eq}$.

the second segment. The third segment was dominated by the low concentrations of small flakes, but the midsize flakes were well represented and the large flakes were also present including aggregates as large as 15 mm.

b. Snowflake mass

Time series of the coefficients, a_v and a_m , of the v - D_{mx} and m - D_{mx} relationships, respectively, reflected the characteristic differences between and within the events. In this study, time series of a_v was constructed for four different D_{mx} - D_{eq} relationships while time series of a_m was presented for four different Best number approaches when $D_{mx} = 1.4D_{eq}$.

Time series of a_v in event 11 reflected the uniform nature of the event where the maximum and minimum a_v values ranged between 0.5 and $1.9 \text{ m s}^{-1} \text{cm}^{-b_v}$ (Fig. 10a). The maximum difference in a_v at a given time occurred between $1.3D_{eq}$ and $1.5D_{eq}$ and was $0.8 \text{ m s}^{-1} \text{cm}^{-b_v}$. Time series of a_m in event 11 had uniform structure throughout the event but there were significant differences in a_m at a given time between the four methods (Fig. 10b). The a_m values were significantly lower for the HW method and the maximum difference in a_m at a given time, $0.005 \text{ g cm}^{-b_m}$, occurred between the HW and MH methods. The MH method resulted in slightly higher a_m values than the BM and KC methods.

Time series of a_v in event 30 reflected the three segments of the event discussed in section 5. The first segment had uniform structure where the maximum and minimum a_v values are bounded between 1.1 and $1.9 \text{ m s}^{-1} \text{cm}^{-b_v}$ (Fig. 11a). The second segments of the storm had high variability where the minimum and maximum a_v values ranged from 1.2 to $4.9 \text{ m s}^{-1} \text{cm}^{-b_v}$. The third segment of the storm had moderate variability with a 0.6 – $2.7 \text{ m s}^{-1} \text{cm}^{-b_v}$ range in a_v . The maximum difference in a_v at a given time was observed between $1.2D_{eq}$ and $1.5D_{eq}$ during the second segment of the event and was $2.5 \text{ m s}^{-1} \text{cm}^{-b_v}$. It should be noted that the exponent (b_v) of the v - D_{mx} relationships was around 0.5 in

the power-law relationships. For a 0.1 cm snowflake with $a_v = 4.9 \text{ m s}^{-1} \text{cm}^{-b_v}$ and $b_v = 0.5$, PIP fall velocity is 1.55 m s^{-1} . Indeed, the visual inspection of velocity tables (not shown) showed that the median PIP fall velocity for the bin centered at 1.1-mm diameter remained less than 2 m s^{-1} during the second segment of the event.

Time series of a_m in event 30 had a similar trend as the time series of a_v for the same event (Fig. 11b). The uniformity and high variability were evident during the first and second segment of the event, respectively, and a_m ranged between 0.002 and 0.06 g cm^{-b_m} during the second segment. The exponent (b_m) of the m - D_{mx} relationship was around 2.6 when a_m had the highest value in this segment. For a 0.1 cm snowflake with $a_m = 0.06 \text{ g cm}^{-b_m}$ and $b_m = 2.6$, mass is 0.00015 g matching well with the mass table (not shown). It should be noted that the HW method resulted in distinctly lower a_m values throughout the event. The maximum difference in a_m at a given time, 0.39 g cm^{-b_m} , was observed between the MH and HW methods during the highly variable second segment and was significantly higher than the difference in event 11. The dependency of the PIP-retrieved mass to the method of derivation has a clear role on the PIP-retrieved SWE that will be discussed later in this paper.

c. Snow water equivalent

Time series of PIP-retrieved and stake field-measured SWE show different degrees of agreement on an event-by-event basis. The PIP-estimated SWE was more sensitive to the method of Re- X numbers relationship than to the choice of D_{mx} - D_{eq} relationship. A separate figure was therefore generated for each of the four Re- X numbers relationships for each event. Each figure includes PIP-retrieved SWE for $D_{mx} = 1.2D_{eq}$ and $D_{mx} = 1.5D_{eq}$. Given the fact that PL09 gauge malfunctioned in several events, the uncorrected and wind-corrected stake field records were taken as a reference.

The two events presented in detail in previous sections showed significant differences for the performance of the PIP-retrieved SWE. Table 3 presents the performance of PIP-retrieved SWE in terms of absolute bias (%). The absolute bias is the difference between the PIP-retrieved and stake field-measured SWE divided by stake field-measured SWE multiplied by 100. The level of agreement is given for each Re- X relationship and the range of the absolute bias represents the agreement among the four different D_{mx} - D_{eq} relationships. For event 11, the PIP-retrieved SWE had better agreements with the wind corrected stake field measurements; the best agreement with the absolute bias of 2.4% occurred when SWE was retrieved with the HW method and $D_{mx} = 1.5D_{eq}$ (Fig. 12).

The PIP-retrieved SWE agreed better with the uncorrected stake field data than the wind corrected stake field data for event 30 (Fig. 13). If the absolute biases $\leq 15\%$, 10% , and 5% are considered as good, very good, and excellent agreements, respectively, PIP-retrieved SWE using the BM method had a very good performance with respect to uncorrected stake field record for all D_{mx} - D_{eq} relationships (Table 3).

TABLE 3. Performance of PIP-retrieved SWE with respect to uncorrected (first row for each event) and wind corrected (second row) stake field measurements. The absolute bias (abs_bias) is given for the range based on $D_{\text{mx}}-D_{\text{eq}}$ relationships for X -Re relationships. The event lowest absolute bias is shown in boldface font. The rows for the two events (11 and 30) discussed in detail are in italics.

Event No.	abs_bias (%; BM)	abs_bias (%; HW)	abs_bias (%; KC)	abs_bias (%; MH)
1	106.0–145.8 29.0–53.9	77.5–84.5 11.2 –15.5	128.1–176.9 42.8–73.4	147.7–202.6 55.1–89.5
2	28.1–43.4 1.0–9.4	7.7–12.3 20.6–23.9	40.6–60.2 0.6 –13.3	52.5–74.9 7.8–23.6
3	53.6–79.9 6.7 –25.0	30.9–34.2 6.7–9.0	71.2–100.5 85.7–119.2	85.7–119.2 29.0–52.3
4	101.8–128.3 5.4–19.3	72.3–86.0 2.8 –10.0	119.7–152.7 14.8–32.0	136.3–176.4 23.4–44.4
5	32.5–48.1 0.1 –11.9	12.2–18.9 9.0–15.2	44.2–63.7 9.0–23.6	55.4–77.9 17.4–34.4
6	1.0–12.7 8.6–19.5	22.7–25.6 28.7–31.4	2.8–11.1 0.0–11.5	3.7–21.0 2.7–11.7
7	0.5 –9.1 17.4–23.8	8.4–18.9 30.6–38.6	7.8–15.9 12.2–18.4	14.8–23.8 6.2–13.0
8	37.1–56.2 2.9 –8.8	17.4–23.1 14.3–18.2	49.6–71.5 4.2–19.4	61.3–86.1 12.3–29.6
9	46.3–66.2 10.3–18.1	19.5–36.1 3.3 –15.1	71.1–81.5 21.5–28.9	84.0–98.7 30.7–41.1
10	61.3–78.8 40.1–55.3	33.3–58.4 15.0–37.6	66.5–86.3 44.6–61.8	75.8–97.4 52.7–71.5
<i>11</i>	<i>81.3–104.1</i> <i>21.2–36.6</i>	<i>53.1–74.7</i> <i>2.4</i> –16.9	<i>89.5–116.5</i> <i>26.8–37.7</i>	<i>100.9–130.2</i> <i>34.4–54.0</i>
12	10.3–18.0 38.3–45.0	27.4–31.8 51.4–54.3	0.4 –9.6 32.7–39.4	2.8–8.6 27.2–35.0
13	1.0 –7.4 37.3–44.7	17.1–23.4 50.4–54.2	1.0–12.8 32.0–39.6	9.0–23.3 26.3–34.9
14	2.0–7.4 10.3–19.9	16.1–20.8 27.4–31.5	0.4–14.3 1.1–13.2	8.3–24.3 0.3 –7.6
15	26.0–36.3 12.8–19.4	1.9–7.8 31.0–37.2	40.0–52.7 2.3–10.4	51.9–66.5 1.8 –6.6
16	23.6–38.7 15.9–25.1	4.2–13.6 31.1–41.9	32.0–48.3 10.1–20.0	41.4–59.2 3.5 –14.3
17	9.8–27.1 30.7–40.1	2.7 –8.0 42.5–49.9	15.6–32.5 27.7–37.0	22.6–41.0 23.1–33.2
18	22.4–36.8 1.0 –6.7	4.9–17.3 10.6–20.0	27.9–45.0 2.5–6.7	35.6–54.1 3.4–17.5
19	6.6–11.1 37.5–40.6	24.4–32.2 49.5–54.7	1.0 –6.6 28.7–33.8	7.9–16.8 21.9–27.8
20	16.8–20.7 27.0–30.7	32.3–41.4 40.6–48.6	6.7–12.5 18.1–23.2	0.9 –4.6 10.3–16.2
21	30.5–35.3 46.4–50.1	45.3–51.4 57.8–62.6	21.6–27.7 39.6–44.3	13.3 –20.3 33.2–38.6
22	32.6–41.5 33.7–42.5	53.1–53.5 53.9–54.2	21.1–32.0 22.4–33.1	9.9 –24.0 11.4–25.3
23	6.3–18.4 33.2–41.8	30.1–31.8 50.1–51.4	2.4–8.3 23.7–34.6	0.6 –18.5 15.5–28.3
24	33.8–53.4 1.5 –13.0	13.3–17.1 13.8–16.6	49.0–74.0 9.8–28.1	62.4–91.4 19.6–41.0
25	19.7–28.4 35.6–42.5	35.8–39.3 48.5–51.2	10.2–15.7 28.0–37.0	2.4 –15.4 21.7–32.1
26	1.1–8.8 14.8–24.0	15.7–20.1 29.7–33.4	3.0–20.1 8.1–13.7	3.6–18.7 1.0 –13.7
27	24.7–41.6 11.1–21.7	8.2–18.7 25.5–32.1	32.7–53.9 3.4–11.5	41.3–64.6 1.1 –11.3
28	58.8–229.8 23.6–156.7	30.6–48.0 1.7 –15.2	69.6–86.0 32.0–44.8	81.7–106.5 41.4–55.2

TABLE 3. (Continued)

Event No.	abs_bias (%; BM)	abs_bias (%; HW)	abs_bias (%; KC)	abs_bias (%; MH)
29	18.0–26.4	39.1–40.6	6.2–16.8	0.3 –8.8
	23.0–30.9	42.8–44.2	11.9–21.9	2.6–14.3
30	1.4 –6.2	18.0–26.5	3.3–15.3	11.8–21.6
	43.5–48.6	55.0–59.7	36.8–43.4	31.4–38.7

In fact, three of the $D_{\text{mx}}-D_{\text{eq}}$ relationship in the BM method and $D_{\text{mx}} = 1.2D_{\text{eq}}$ in the KC method resulted in excellent performance for the PIP-retrieved SWE. It was expected that the PIP-retrieved SWE would have a better agreement with the wind corrected gauge records in windy conditions. Event 30 was moderately windy with higher median and maximum wind speeds than the event 11. Yet the PIP-retrieved SWE agreed better with the uncorrected stake field record.

7. Overall comparisons

An overall performance of the PIP-retrieved SWE was evaluated based on its absolute bias with respect the uncorrected and wind corrected stake field records for the 30 events. Additionally, time series of each event were visually inspected to ensure that any agreement at the end of the event was result of cancellation between two disagreements

(i.e., the gauge was higher in one segment and PIP was higher in another segment of event). The minimum absolute bias was sought among the four $D_{\text{mx}}-D_{\text{eq}}$ relationship based on the PIP-retrieved SWE and stake field record for a given Re- X method in each event.

Figures 14 and 15 present the scatter diagrams of PIP-retrieved SWE and stake field totals without and with wind corrections, respectively, when the BM, HW, KC, and MH methods are used. The Pearson correlation coefficient, bias, and absolute bias are included. Considering the uncorrected stake field record as a reference, the $D_{\text{mx}} = 1.2D_{\text{eq}}$ relationship had the minimum absolute bias for most of the events when the BM, KC, and MH methods were used (Fig. 14). For the HW method, the minimum absolute bias was obtained when $D_{\text{mx}} = 1.5D_{\text{eq}}$ was used for most of the events. Overall, the PIP-retrieved SWE was overestimated when BM, KC, and MH methods were used and underestimated when HW

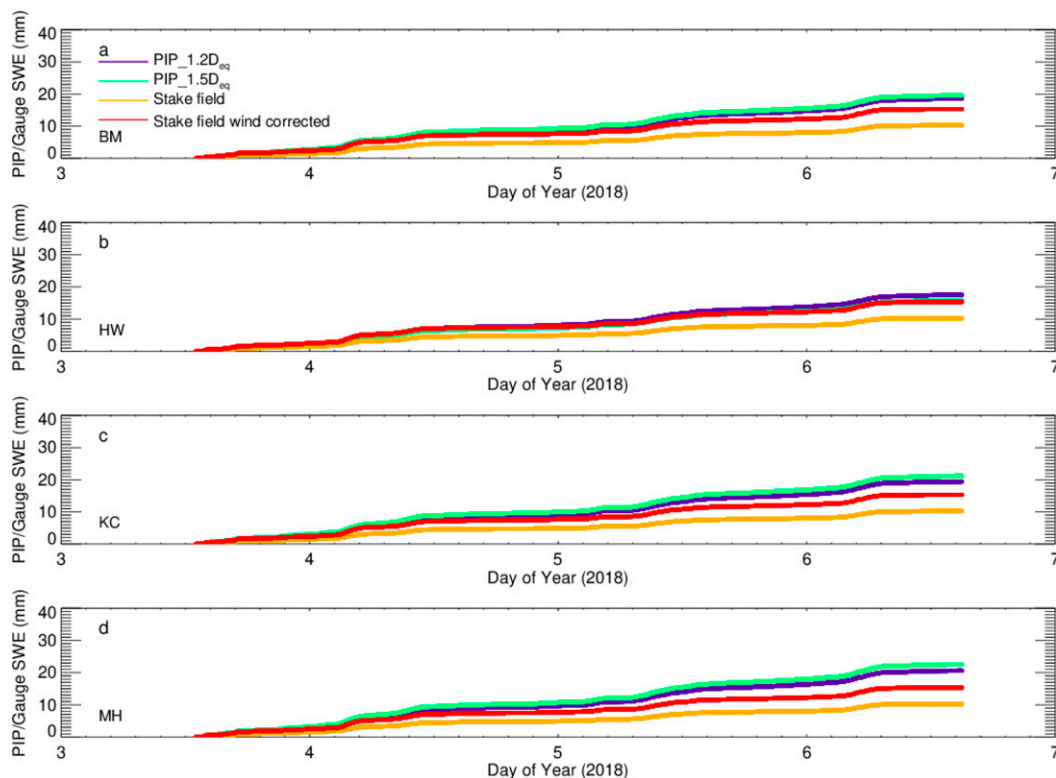


FIG. 12. Time series of accumulative snow water equivalent (SWE) for event 11 for uncorrected and wind-corrected NWS snow stake field observations and for (a) BM, (b) HW, (c) KC, and (d) MH method-based PIP calculations and when PIP maximum dimension is equal to $1.2D_{\text{eq}}$ and $1.5D_{\text{eq}}$.

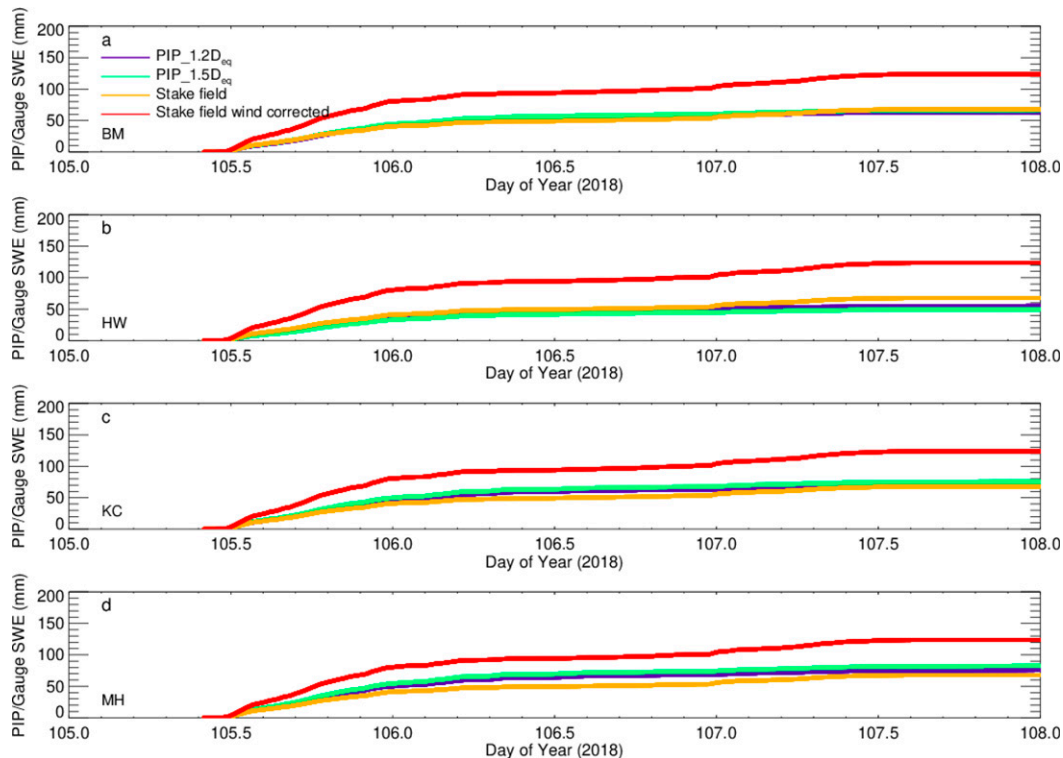


FIG. 13. Time series of accumulative snow water equivalent (SWE) for event 30 for uncorrected and wind-corrected NWS snow stake field observations and for (a) BM, (b) HW, (c) KC, and (d) MH method-based PIP calculations and when PIP maximum dimension is equal to $1.2D_{eq}$ and $1.5D_{eq}$.

method was used. The BM method based PIP-retrieved SWE had the best performance with an absolute bias of 19%, while the absolute biases were 2.4%, 3.5%, and 8.3% higher when the KC, HW, and MH methods were used.

The absolute biases were higher except for the MH method when the wind corrected gauge record was considered as a reference. The MH method based PIP-retrieved SWE had the best performance with absolute bias of 20.7% (Fig. 15). Overall, PIP-retrieved SWE was underestimated with respect to the wind corrected gauge record regardless of which of the four method was used. The bias difference between the uncorrected and corrected gauge references was the lowest for the HW method (28.9%) and highest for the MH method (38.2%). In terms of absolute bias difference, however, the HW and KC methods resulted in the maximum (18%) and minimum (2.1%) differences between the two references, respectively.

Figure 16 presents the scatter diagrams of PIP-retrieved SWE and stake field totals without and with wind correction, respectively. In these figures, the PIP-retrieved SWE method that had the best agreement with respect to the reference gauge was chosen. For most of the events, the HW and MH methods resulted in the best agreement with respect to uncorrected and wind corrected gauges, respectively. The agreement was better with respect to the uncorrected gauge totals with an absolute bias of 7.1%. The comparison of PIP-retrieved SWE with either uncorrected or wind corrected

stake field records resulted in an excellent agreement with an absolute bias of 2.0%. On event-by-event basis, the PIP-retrieved SWE was in a good agreement, $\leq 15\%$, with respect to either uncorrected or wind corrected stake field measurements (Table 3). Realistically, the wind corrected gauge record should be used above a certain wind speed threshold. In this study, 12 out of 30 events had a better agreement when uncorrected gauge record was the reference and half of those events occurred when the median wind speed was moderate ($3\text{--}6\text{ m s}^{-1}$) (Table 3).

8. Conclusions

One of main achievements of precipitation related field studies is to collect sufficient samples of data. There are perhaps two common obstacles that may prevent the collection of sufficient data: 1) an unexpected drought and 2) instrument malfunction. During the 2017/18 winter, the PIP functioned nearly uninterrupted collecting 2345.8 mm of geometric DP in 499 h under frigid weather conditions where the wet-bulb temperature dipped below -20°C . PIP is a low-cost and robust disdrometer. Considering its continuous and unattended operation, it is expected that PIP would be very useful for operational use as part of the automated surface stations.

This study focused on the methodology for deriving SWE from PIP particle size and fall velocity measurements.

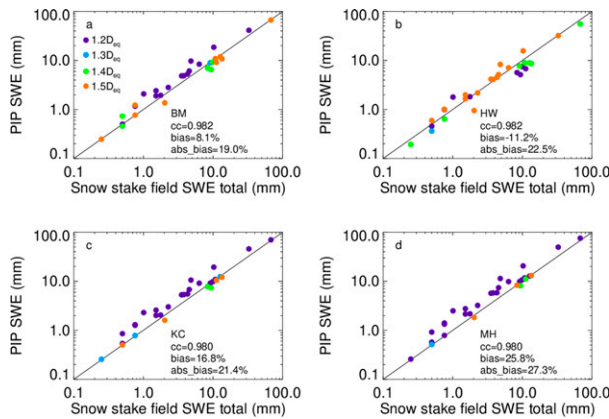


FIG. 14. Comparison of PIP-retrieved and NWS stake field-measured (without wind correction) snow water equivalent (SWE) event totals for (a) BM, (b) HW, (c) KC, and (d) MH method-based PIP calculations and for the best agreement among the four PIP D_{mx} - D_{eq} relationships ($1.2D_{eq}$, $1.3D_{eq}$, $1.4D_{eq}$, and $1.5D_{eq}$). The correlation coefficient (cc), bias, and absolute bias between the two estimated and observed variables are also in given.

The motivation was to construct the validation product for the GPM active and passive sensor-based precipitation estimate in snow. The GPM algorithms also seek an appropriate Ze(SWER) relationships for the DPR measurements. This is a challenging task due to the complexity of the physics of a snowflake considering its size, density, habit, composition, and related scattering properties. Despite measurement uncertainties and the assumptions in calculations of snowflake mass, it is remarkable to achieve a very good agreement between the PIP-retrieved and stake field-measured SWE. The absolute bias between the estimate and reference SWE was less than 15% for at least one of the Re- X relationship and D_{mx} - D_{eq} pair for all of the 30 events used in this study.

The diversity between the two events and within the different segments of the second event are the evidence of the complex nature of falling snow. The nearly nonstop falling snow over 3 days with northwesterly wind, the absence of large flakes ($D_{eq} \geq 5$ mm) in PIP observations, and the shallow (<1.5-km height) reflectivity in MRR observations were the characteristics of the first event. These features coincided with the 19–20 November 2016 lake-effect snowstorm that was reported in Kulie et al. (2021). The high accumulations with abrupt wind direction change from northeast to northwest, the presence of large flakes in PIP observations, and the combination of deep and shallow MRR reflectivity regimes were the characteristics of the second event. These features coincided with the 10–12 November 2014 lake-enhanced snowstorm that was reported in Kulie et al. (2021).

This study boosts our confidence to derive the Ze(SWER) relationship using PIP measurements. Perhaps one caveat in PIP measurements is the determination of the habit and composition (i.e., degree of riming) of the individual snowflakes.

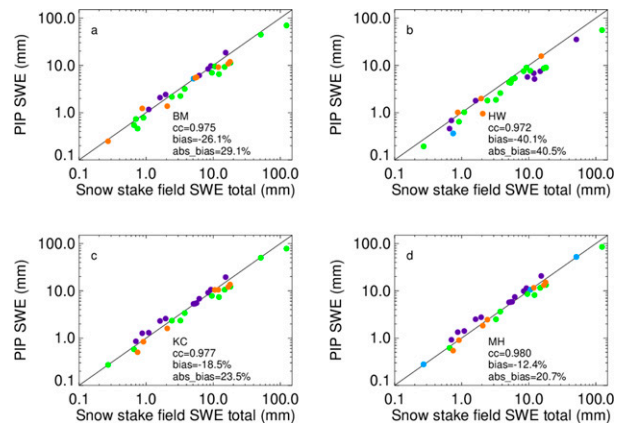


FIG. 15. Comparison of PIP-retrieved and NWS stake field-measured (with wind correction) SWE event totals for (a) BM, (b) HW, (c) KC, and (d) MH method-based PIP calculations and for the best agreement among the four PIP D_{mx} - D_{eq} relationships ($1.2D_{eq}$, $1.3D_{eq}$, $1.4D_{eq}$, and $1.5D_{eq}$). The cc, bias, and absolute bias between the two estimated and observed variables are also in given.

Collocated PIP and MASC measurement would be beneficial to derive more robust Ze(SWER) relation for different habits and composition.

Acknowledgments. Comments from S. Joseph Munchak and Robert Meneghini of NASA Goddard Space Flight Center, Charles (Chip) Helms of Universities Space Research Association, and Liang Liao of Morgan State University are highly appreciated. Discussions with Norm Wood of University of Wisconsin–Madison on PIP data processing were very helpful. Leo Pio D’Adderio of National Research Council of Italy provided Fig. 1 of this study. Thanks to the National Weather Service in Marquette, Michigan, for hosting and maintaining the suite of instruments used in this work and sharing meteorological data. Thanks to the National Aeronautics and Space Administration Goddard Space Flight Center Wallops Flight Facility and the Global Precipitation Measurement (GPM) program for providing the PIP, Pluvio, and PARSIVEL instruments used in this work. Acknowledgments extend to three anonymous reviewers for their constructive comments. This study is partially supported by the NASA award (80NCCS19M0139) under Patrick N. Gatlin of NASA Marshall Space Flight Center, principal investigator. The instrument deployment and data processing for the observations from the Marquette snowfall suite are supported by NASA Grant 80NSSC18K0701 and NOAA Grant NA15NES4320001. Claire Pettersen’s efforts on this work are supported by NASA Grant 80NSSC19K0712, and Mark Kulie’s efforts are supported by NASA PMM Grant 80NSSC20K0982. Annakaia von Lerber is funded by the Academy of Finland postdoctoral scholarship (333901). The scientific results and conclusions, as well as any views or opinions expressed herein, are those of the authors and do not necessarily reflect those of NOAA or the Department of Commerce.

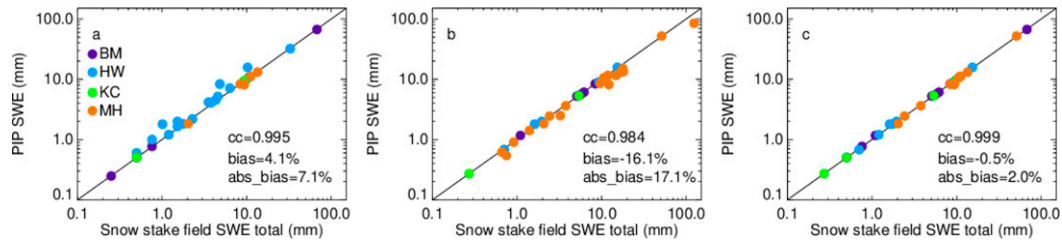


FIG. 16. Comparison of PIP-retrieved and NWS snow stake field-measured SWE event totals (a) without wind correction, (b) with wind correction, (c) with or without wind correction for the best agreement among the four PIP mass estimation methods (BM, HW, KC, and MH) and the four PIP $D_{mx}(D_{eq})$ relationships ($1.2D_{eq}$, $1.3D_{eq}$, $1.4D_{eq}$, and $1.5D_{eq}$, not shown). The cc, bias, and absolute bias between the two estimated and observed variables are also in given.

APPENDIX

Variable Definitions

a. Descriptors of particle size

D_{eq} : Equivalent diameter; it is a Waddell disk diameter that was described as the diameter of the disk with the same area as the particle in National Instruments IMAQ manual, which describes D_{eq} equal to $2(\text{area}/\pi)^{0.5}$, where area is the total area of shadowed pixels bounded by a box

D_{min} : Minimum particle size based on D_{eq} measurements

D_{max} : Maximum particle size based on D_{eq} measurements

D_{mx} : Maximum dimension of the particle; it is prescribed as a function of D_{eq} as in Eq. (5) in this study

D_{mass} : Mass weighted mean diameter

D_{mass*} : Melted value of D_{mass} as in Liao et al. (2016) and Chase et al. (2020)

b. Size distribution and integral parameters

N_T : Total particle concentration that is given as number of particle per cubic volume of air

N_T^* : Normalized intercept parameter of gamma size distribution; it is the ratio of N_T to D_{mass}

μ : Shape parameter of gamma size distribution

SR: Snow rate; this is intensity of falling snow without melting

DP: Snow depth; this is accumulative snowfall without melting or compression on the ground

SWER: Melted equivalent snow rate

SWE: Melted equivalent of falling snow

RR: Rain rate; Precipitation rate

Ze: Radar reflectivity calculated by a disdrometer

c. Velocity, mass, and related parameters

v : Fall velocity of a snowflake

A_v : Coefficient of the v - D_{mx} power-law relationship

B_v : Exponent of the v - D_{mx} power-law relationship

M : Mass of a snowflake

A_m : Coefficient of the m - D_{mx} power-law relationship

B_m : Exponent of the m - D_{mx} power-law relationship

Re: Reynolds number

η : Dynamic viscosity

ρ_a : Density of air at the ground level

X : Best number

δ_0 : Boundary layer thickness

C_D : Drag coefficient

G : Gravitational constant

A_e : Effective particle area

A : The area of the smallest circle or ellipse which contains A_e

d. Environmental variables

WSP_{med} : Median wind speed

WSP_{max} : Maximum wind speed

WB_{med} : Median wet-bulb temperature

WB_{max} : Maximum wet-bulb temperature

U : 30-min surface average wind speed

T_a : 30-min-average surface air temperature

REFERENCES

- Battaglia, A., E. Rustemeier, A. Tokay, U. Blahak, and C. Simmer, 2010: PARSIVEL snow observations: A critical assessment. *J. Atmos. Oceanic Technol.*, **27**, 333–344, <https://doi.org/10.1175/2009JTECHA1332.1>.
- Böhm, H., 1989: A general equation for the terminal fall speed of solid hydrometeors. *J. Atmos. Sci.*, **46**, 2419–2427, [https://doi.org/10.1175/1520-0469\(1989\)046<2419:AGEFTT>2.0.CO;2](https://doi.org/10.1175/1520-0469(1989)046<2419:AGEFTT>2.0.CO;2).
- Brandes, E. A., K. Ikeda, G. Zhang, M. Schönhuber, and R. M. Rasmussen, 2007: A statistical and physical description of hydrometeor distributions in Colorado snowstorms using a video disdrometer. *J. Appl. Meteor. Climatol.*, **46**, 634–650, <https://doi.org/10.1175/JAM2489.1>.
- Buković, P., A. Ryzhkov, D. Zrnić, and G. Zhang, 2018: Polarimetric radar relations for quantification of snow based on disdrometer data. *J. Appl. Meteor. Climatol.*, **57**, 103–120, <https://doi.org/10.1175/JAMC-D-17-0090.1>.
- , —, and —, 2020: Polarimetric relations for snow estimation—Radar verification. *J. Appl. Meteor. Climatol.*, **59**, 991–1009, <https://doi.org/10.1175/JAMC-D-19-0140.1>.
- Chase, R. J., S. W. Nesbitt, and G. M. McFarquhar, 2020: Evaluation of the microphysical assumptions within GPM-DPR using ground-based observations of rain and snow. *Atmosphere*, **11**, 619, <https://doi.org/10.3390/atmos11060619>.
- Chen, S., J. J. Gourley, Y. Hong, Q. Cao, N. Carr, P. E. Kirstetter, J. Zhang, and Z. Flamig, 2016: Using citizen science reports

- to evaluate estimates of surface precipitation type. *Bull. Amer. Meteor. Soc.*, **97**, 187–193, <https://doi.org/10.1175/BAMS-D-13-00247.1>.
- Falconi, M. T., A. von Lerber, D. Ori, F. S. Marzano, and D. Moisseev, 2018: Snowfall retrieval at X, Ka and W bands: Consistency of backscattering and microphysical properties using BAECC ground-based measurements. *Atmos. Meas. Tech.*, **11**, 3059–3079, <https://doi.org/10.5194/amt-11-3059-2018>.
- Field, P. R., A. J. Heymsfield, and A. Bansemer, 2006: Shattering and particle interarrival times measured by optical array probes in ice clouds. *J. Atmos. Oceanic Technol.*, **23**, 1357–1371, <https://doi.org/10.1175/JTECH1922.1>.
- Garrett, T. J., C. Fallgatter, K. Shkurko, and D. Howlett, 2012: Fall speed measurement and high-resolution multi-angle photography of hydrometeors in free fall. *Atmos. Meas. Tech.*, **5**, 2625–2633, <https://doi.org/10.5194/amt-5-2625-2012>.
- Gunn, K. L. S., and J. S. Marshall, 1958: The distribution with size of aggregate snowflakes. *J. Meteor.*, **15**, 452–461, [https://doi.org/10.1175/1520-0469\(1958\)015<0452:TDWSOA>2.0.CO;2](https://doi.org/10.1175/1520-0469(1958)015<0452:TDWSOA>2.0.CO;2).
- Heymsfield, A. J., and C. D. Westbrook, 2010: Advancements in the estimation of ice particle fall speeds using laboratory and field measurements. *J. Atmos. Sci.*, **67**, 2469–2482, <https://doi.org/10.1175/2010JAS379.1>.
- Huang, G.-J., V. N. Bringi, R. Cifelli, D. Hudak, and W. A. Petersen, 2010: A methodology to derive radar reflectivity–liquid equivalent snow rate relations using C-band radar and a 2D video disdrometer. *J. Atmos. Oceanic Technol.*, **27**, 637–651, <https://doi.org/10.1175/2009JTECHA1284.1>.
- , —, D. Moisseev, W. A. Petersen, L. Bliven, and D. Hudak, 2015: Use of 2D-video disdrometer to derive mean density–size and Ze–SR relations: Four snow cases from the light precipitation validation experiment. *Atmos. Res.*, **153**, 34–48, <https://doi.org/10.1016/j.atmosres.2014.07.013>.
- Khvorostyanov, V., and J. A. Curry, 2005: Fall velocities of hydrometeors in the atmosphere refinements to a continuous analytical power law. *J. Atmos. Sci.*, **62**, 4343–4357, <https://doi.org/10.1175/JAS3622.1>.
- Kirstetter, P. E., J. J. Gourley, Y. Hang, J. Zhang, S. Moazami-goodarzi, C. Langston, and A. Arthur, 2015: Probabilistic precipitation rate estimates with ground-based radar networks. *Water Resour. Res.*, **51**, 1422–1442, <https://doi.org/10.1002/2014WR015672>.
- Kneifel, S., A. von Lerber, J. Tiira, D. Moisseev, P. Kollias, and J. Leinonen, 2015: Observed relations between snowfall microphysics and triple-frequency radar measurements. *J. Geophys. Res. Atmos.*, **120**, 6034–6055, <https://doi.org/10.1002/2015JD023156>.
- Kochendorfer, J., and Coauthors, 2017: Analysis of single-Alter shielded and unshielded measurements of mixed and solid precipitation from WMO-SPICE. *Hydrol. Earth Syst. Sci.*, **21**, 3525–3542, <https://doi.org/10.5194/hess-21-3525-2017>.
- Kulie, M. S., and Coauthors, 2021: Snowfall in the northern Great Lakes: Lessons learned from a multi-sensor observatory. *Bull. Amer. Meteor. Soc.*, **102**, E1317–E1339, <https://doi.org/10.1175/BAMS-D-19-0128.1>.
- Lau, K. M. Y., and Coauthors, 2000: A report of the field observations and early results of the South China Sea Monsoon Experiment (SCSMEX). *Bull. Amer. Meteor. Soc.*, **81**, 1261–1270, [https://doi.org/10.1175/1520-0477\(2000\)081<1261:AROTFO>2.3.CO;2](https://doi.org/10.1175/1520-0477(2000)081<1261:AROTFO>2.3.CO;2).
- Lee, M., and V. Chandrasekar, 2019: Ground validation of surface snowfall algorithm in GPM Dual-Frequency Precipitation Radar. *J. Atmos. Oceanic Technol.*, **36**, 607–619, <https://doi.org/10.1175/JTECH-D-18-0098.1>.
- Leinonen, J., S. Kneifel, D. Moisseev, J. Tyynelä, S. Tanelli, and T. Nousiainen, 2012: Evidence of nonspherical behavior in millimeter-wavelength radar observations of snowfall. *J. Geophys. Res.*, **117**, D18205, <https://doi.org/10.1029/2012JD017680>.
- Li, H., D. Moisseev, and A. von Lerber, 2018: How does riming affect dual-polarization radar observations and snowflake shape? *J. Geophys. Res. Atmos.*, **123**, 6070–6081, <https://doi.org/10.1029/2017JD028186>.
- , J. Tiira, A. von Lerber, and D. Moisseev, 2020: Towards the connection between snow microphysics and melting layer: Insights from multifrequency and dual-polarization radar observations during BAECC. *Atmos. Chem. Phys.*, **20**, 9547–9562, <https://doi.org/10.5194/acp-20-9547-2020>.
- Liao, L., R. Meneghini, A. Tokay, and L. F. Bliven, 2016: Retrieval of snow properties for Ku- and Ka-band dual-frequency radar. *J. Appl. Meteor. Climatol.*, **55**, 1845–1858, <https://doi.org/10.1175/JAMC-D-15-0355.1>.
- Magono, C., and T. Nakamura, 1965: Aerodynamic studies of falling snowflakes. *J. Meteor. Soc. Japan*, **43**, 139–147, <https://doi.org/10.2151/jmsj1965.43.3.139>.
- Matrosov, S. Y., 2007: Modeling backscatter properties of snowfall at millimeter wavelengths. *J. Atmos. Sci.*, **64**, 1727–1736, <https://doi.org/10.1175/JAS3904.1>.
- Mitchell, D. L., and A. J. Heymsfield, 2005: Refinements in the treatment of ice particle terminal velocities, highlighting aggregates. *J. Atmos. Sci.*, **62**, 1637–1644, <https://doi.org/10.1175/JAS3413.1>.
- Moisseev, D., A. von Lerber, and J. Tiira, 2017: Quantifying the effect of riming on snowfall using ground-based observations. *J. Geophys. Res. Atmos.*, **122**, 4019–4037, <https://doi.org/10.1002/2016JD026272>.
- National Instruments, 2004: IMAQ vision for LabVIEW user manual. National Instruments Doc., 141 pp., <https://www.ni.com/pdf/manuals/371007a.pdf>.
- Newman, A. J., P. A. Kucera, and L. F. Bliven, 2009: Presenting the Snowflake Video Imager (SVI). *J. Atmos. Oceanic Technol.*, **26**, 167–179, <https://doi.org/10.1175/2008JTECHA1148.1>.
- Pettersen, C., M. S. Kulie, L. F. Bliven, A. J. Merrelli, W. A. Petersen, T. J. Wagner, D. B. Wolff, and N. B. Wood, 2020a: A composite analysis of snowfall modes from four winter seasons in Marquette, Michigan. *J. Appl. Meteor. Climatol.*, **59**, 103–124, <https://doi.org/10.1175/JAMC-D-19-0099.1>.
- , and Coauthors, 2020b: Introducing the Precipitation Imaging Package: Assessment of microphysical and bulk characteristics of snow. *Atmosphere*, **11**, 785, <https://doi.org/10.3390/atmos11080785>.
- Rasmussen, R., and Coauthors, 2012: How well are we measuring snow? The NOAA/FAA/NCAR winter precipitation test bed. *Bull. Amer. Meteor. Soc.*, **93**, 811–829, <https://doi.org/10.1175/BAMS-D-11-00052.1>.
- Skofronick-Jackson, G., and Coauthors, 2015: Global Precipitation Measurement Cold Season Precipitation Experiment (GCPEX): For measurement's sake, let it snow. *Bull. Amer. Meteor. Soc.*, **96**, 1719–1741, <https://doi.org/10.1175/BAMS-D-13-00262.1>.
- , and Coauthors, 2017: The Global Precipitation Measurement (GPM) mission for science and society. *Bull. Amer. Meteor. Soc.*, **98**, 1679–1695, <https://doi.org/10.1175/BAMS-D-15-00306.1>.

- Souvereinjs, N., A. Gossart, S. Lhermitte, I. V. Gorodetskaya, S. Kneifel, M. Maahn, F. L. Bliven, and N. P. M. van Lipzig, 2017: Estimating radar reflectivity–snowfall rate relationships and their uncertainties over Antarctica by combining disdrometer and radar observations. *Atmos. Res.*, **196**, 211–223, <https://doi.org/10.1016/j.atmosres.2017.06.001>.
- Szyrmer, W., and I. Zawadzki, 2010: Snow studies. Part II: Average relationship between mass of snowflakes and their terminal fall velocity. *J. Atmos. Sci.*, **67**, 3319–3335, <https://doi.org/10.1175/2010JAS3390.1>.
- Tiira, J., D. N. Moiseev, A. von Lerber, D. Ori, A. Tokay, L. F. Bliven, and W. Petersen, 2016: Ensemble mean density and its connection to other microphysical properties of falling snow as observed in southern Finland. *Atmos. Meas. Tech.*, **9**, 4825–4841, <https://doi.org/10.5194/amt-9-4825-2016>.
- Tokay, A., P. G. Bashor, E. Habib, and T. Kasparis, 2008: Raindrop size distribution measurements in tropical cyclones. *Mon. Wea. Rev.*, **136**, 1669–1685, <https://doi.org/10.1175/2007MWR2122.1>.
- , W. A. Petersen, P. Gatlin, and M. Wingo, 2013: Comparison of raindrop size distribution measurements by collocated disdrometers. *J. Atmos. Oceanic Technol.*, **30**, 1672–1690, <https://doi.org/10.1175/JTECH-D-12-00163.1>.
- , D. B. Wolff, and W. A. Petersen, 2014: Evaluation of the new version of the laser-optical disdrometer, OTT PARSI-VEL². *J. Atmos. Oceanic Technol.*, **31**, 1276–1288, <https://doi.org/10.1175/JTECH-D-13-00174.1>.
- Tyynelä, J., and V. Chandrasekar, 2014: Characterizing falling snow using multifrequency dual-polarization measurements. *J. Geophys. Res. Atmos.*, **119**, 8268–8283, <https://doi.org/10.1002/2013JD021369>.
- , and A. von Lerber, 2019: Validation of microphysical snow models using in situ, multifrequency, and dual-polarization radar measurements in Finland. *J. Geophys. Res. Atmos.*, **124**, 13 273–13 290, <https://doi.org/10.1029/2019JD030721>.
- von Lerber, A., D. Moiseev, F. Bliven, W. Petersen, A.-M. Harri, and V. Chandrasekar, 2017: Microphysical properties of snow and their link to Ze–S relations during BAECC 2014. *J. Appl. Meteor. Climatol.*, **56**, 1561–1582, <https://doi.org/10.1175/JAMC-D-16-0379.1>.
- , —, D. A. Marks, W. Petersen, A. M. Harri, and V. Chandrasekar, 2018: Validation of GMI snowfall observations by using a combination of weather radar and surface measurements. *J. Appl. Meteor. Climatol.*, **57**, 797–820, <https://doi.org/10.1175/JAMC-D-17-0176.1>.
- Wood, N. B., T. S. L’Ecuyer, F. L. Bliven, and G. L. Stephens, 2013: Characterization of video disdrometer uncertainties and impacts on estimates of snowfall rate and radar reflectivity. *Atmos. Meas. Tech.*, **6**, 3635–3648, <https://doi.org/10.5194/amt-6-3635-2013>.
- , —, A. J. Heymsfield, G. L. Stephens, D. R. Hudak, and P. Rodriguez, 2014: Estimating snow microphysical properties using collocated multi-sensor observations. *J. Geophys. Res. Atmos.*, **119**, 8941–8961, <https://doi.org/10.1002/2013JD021303>.
- , —, —, and —, 2015: Microphysical constraints on millimeter-wavelength scattering properties of snow particles. *J. Appl. Meteor. Climatol.*, **54**, 909–931, <https://doi.org/10.1175/JAMC-D-14-0137.1>.
- Yang, D., 2014: Double fence intercomparison reference (DFIR) versus bush gauge for “true” snowfall measurement. *J. Hydrol.*, **509**, 94–100, <https://doi.org/10.1016/j.jhydrol.2013.08.052>.
- Yuter, S. E., D. E. Kingsmill, L. B. Nance, and M. Löffler-Mang, 2006: Observations of precipitation size and fall speed characteristics within coexisting rain and wet snow. *J. Appl. Meteor. Climatol.*, **45**, 1450–1464, <https://doi.org/10.1175/JAM2406.1>.
- Zhang, J., and Coauthors, 2016: Multi-Radar Multi-Sensor (MRMS) quantitative precipitation estimation: Initial operating capabilities. *Bull. Amer. Meteor. Soc.*, **97**, 621–638, <https://doi.org/10.1175/BAMS-D-14-00174.1>.